

High-Resolution *Chandra* X-ray Imaging and Spectroscopy of the σ Orionis Cluster

Stephen L. Skinner and Kimberly R. Sokal

CASA, Univ. of Colorado, Boulder, CO 80309-0389

David H. Cohen

Dept. of Physics and Astronomy, Swarthmore College, Swarthmore, PA 19081

Marc Gagné

Dept. of Geology and Astronomy, West Chester Univ., West Chester, PA 19383-2130

Stanley P. Owocki and Richard D. Townsend

Bartol Research Inst., Univ. of Delaware, Newark, DE 19716

ABSTRACT

We present results of a 90 ksec *Chandra* X-ray observation of the young σ Orionis cluster (age ~ 3 Myr). This observation provides high-resolution grating spectra of the massive central OB star σ Ori AB (O9.5V + B0.5V) capable of stringently testing wind-shock X-ray emission models. We also analyze the high spatial resolution zero-order image of the central cluster region captured on the ACIS-S CCD detector.

Chandra detected 42 X-ray sources on the primary CCD (ACIS-S3), including low-mass M-type stars down to $\approx 0.2 M_{\odot}$. All but five of the detections have near-IR or optical counterparts and about one-fourth of the X-ray sources are variable. Most of the detections have X-ray properties and near-IR colors that are consistent with normally-reddened or moderately-reddened low-mass K and M-type stars. We present the first X-ray spectrum of the unusual infrared source IRS1, located $\approx 3''$ north of σ Ori AB. Its X-ray properties and fan-shaped mid-IR morphology suggest it is an embedded low mass T Tauri star whose disk/envelope is being photo-evaporated by the strong radiation field of σ Ori AB.

Chandra detected the massive binary system σ Ori AB, the magnetic B star σ Ori E, and the B5V binary system HD 37525. The X-ray emission of σ Ori AB is exceptional, being the most luminous and the softest source (kT ≈ 0.3 keV) in the field. Its emission lines have no significant asymmetries or centroid shifts

relative to laboratory values and are moderately broadened to $\text{HWHM} \approx 264 \text{ km s}^{-1}$, or about one-fourth the terminal wind speed. Forbidden lines in He-like ions are formally undetected, implying strong UV suppression. The Mg XI triplet forms in the wind acceleration zone within one stellar radius above the surface. These X-ray properties are consistent in several respects with the predictions of radiative wind shock theory for an optically thin wind, but explaining the narrow line widths presents a challenge to the theory.

Subject headings: open clusters and associations: individual (σ Orionis) — stars: formation — stars: individual (σ Orionis AB) — stars: pre-main-sequence — X-rays: stars

1. Introduction

Sensitive X-ray grating observations of massive OB stars with *Chandra* and *XMM-Newton* during the past several years have provided a wealth of new data that is improving our understanding of the physical processes that produce their X-ray emission. Luminous OB stars are not expected to have the outer convection zones needed to sustain internally-generated magnetic fields and solar-like (coronal) X-ray emission. Thus, their X-ray emission has generally been attributed to wind shocks.

Theoretical models have attempted to explain the X-ray emission of *single* massive OB stars in terms of X-ray emitting shocks distributed throughout their powerful winds that form as a result of line-driven flow instabilities (Lucy & White 1980; Lucy 1982; ; Feldmeier et al. 1997; Owocki, Castor, & Rybicki 1988). The radiative wind shock emission is predicted to be soft ($\text{kT} \ll 1 \text{ keV}$), in contrast to the harder emission ($\text{kT} \gtrsim 2 \text{ keV}$) that has been detected in some massive colliding wind binaries and in a few OB stars with strong $\sim \text{kG}$ magnetic fields whose winds are magnetically-confined (Sec. 3.7.2). X-ray grating observations provide crucial information on line shapes, widths, centroids, and fluxes needed to test wind shock models.

Grating observations of a limited sample of O and early B-type stars have provided some support for the radiative wind shock picture. Perhaps the support so far comes from the O4f star ζ Pup, which has a high mass-loss rate $\log \dot{M} \sim -5.3 \text{ M}_{\odot} \text{ yr}^{-1}$ (Pauldrach et al. 1994). Its X-ray emission lines are asymmetric with blueshifted centroids and are quite broad with half-width half-maximum values $\text{HWHM} \sim 900 \text{ km s}^{-1}$, equivalent to $\approx 40\%$ of the terminal wind speed (Cassinelli et al. 2001; Kahn et al. 2001; Kramer et al. 2003). The blueshifted asymmetry is predicted by radiative wind shock models of optically thick winds where the

redward part of the line is attenuated from receding wind material on the far side of the star (Owocki & Cohen 2001). However, the observational picture is complex as illustrated by the O9 supergiant ζ Ori, whose emission lines are also very broad but unshifted and nearly symmetric (Waldron & Cassinelli 2001).

For late O and early B-type stars with lower mass-loss rates than O supergiants, clear confirmation of radiative wind shock theory has been more difficult to obtain. Grating spectra of the Orion belt eclipsing binary system δ Ori (O9.5 II + B0.5 III; $\log \dot{M} \sim -6$. $M_{\odot} \text{ yr}^{-1}$; Miller et al. 2002) reveal cool plasma at $kT \sim 0.3$ keV, and symmetric unshifted emission lines with $\text{HWHM} \sim 430 \text{ km s}^{-1}$, or $\approx 22\%$ of the terminal wind speed. The dominant cool plasma is compatible with a shock origin and symmetric unshifted lines are predicted by radiative wind shock simulations for an optically thin wind (MacFarlane et al. 1991; Owocki & Cohen 2001). However, Miller et al. raised some questions about the surprising narrowness and symmetry of the lines in the framework of radiative wind shock models. An even more extreme case is the early B giant β Cru (B0.5 III; $\log \dot{M} \sim -8$. $M_{\odot} \text{ yr}^{-1}$; Cohen et al. 2008). It also has a low plasma temperature and symmetric unshifted lines which are quite narrow ($\text{HWHM} \sim 150 \text{ km s}^{-1}$). Cohen et al. concluded that the narrow lines were difficult to understand in the framework of radiative wind shock theory for fast winds.

Only a handful of X-ray grating observations of OB stars have been obtained and observations of a broader sample of objects are needed to clarify how X-ray properties vary with spectral type, luminosity class, and mass-loss parameters. The Orion complex is particularly well-suited to observational tests of X-ray emission models in massive young stars because of its relative proximity and large concentration of very young OB stars. It is the closest giant molecular cloud containing young massive stars. However, the density of young stars in Orion is high and the deep *Chandra* observation of the Orion Nebula obtained in the COUP project detected more than 1400 X-ray sources (Getman et al. 2005). *Chandra's* superb angular resolution is clearly an advantage in deep X-ray observations of Orion in order to avoid source misidentification.

A promising target for exploring X-ray production in young high-mass stars is σ Orionis AB (Table 1), the focus of this study. It is located in the Ori OB1b association and is quite young with an estimated age of 3 ± 2 Myr (Caballero 2007a and references therein; Caballero 2008). The *Hipparcos* distance is 352_{-85}^{+166} pc, which we adopt here. A slightly smaller value of 334_{-22}^{+25} pc was recently obtained by Caballero (2008) who also noted that $d \sim 385$ pc is possible if σ Ori AB is a triple system. For comparison, recent distance measurements of the Orion Nebula cluster give 389_{-21}^{+24} pc (Sandstrom et al. 2007), 392_{-32}^{+32} pc (Jeffries 2007), and 414 ± 7 pc (Menten et al. 2007).

σ Ori AB is a visual binary consisting of a O9.5V primary and a B0.5V companion separated by 0."25 (Mason et al. 1998) and is known to be a bright X-ray source (Berghöfer & Schmitt 1994; Berghöfer, Schmitt, & Cassinelli 1996). The A and B components cannot be separated by existing X-ray telescopes. At a distance of 352 pc, the angular separation equates to a projected linear separation of 88 AU, or 2101 R_{O-star} (Table 1). The extinction toward σ Ori AB is low with $E(B-V) = 0.05 - 0.07$ (Table 1), thus minimizing interstellar absorption of any soft X-rays that might be produced in stellar wind shocks. In terms of wind strength, σ Ori A provides a good comparison with observations of other OB stars. Its wind is much weaker than the O4f star ζ Pup, and its mass-loss rate falls roughly in between that of the moderate wind source δ Ori and the weak wind source β Cru.

There is additional interest in σ Ori because it is surrounded by a cluster of several hundred young stars, originally discovered in *ROSAT* X-ray observations (Walter et al. 1997). *Spitzer* mid-IR observations have identified more than 300 cluster members, with a disk fraction of $\approx 35\%$ in low-mass stars (Hernández et al. 2007). A similar disk fraction was found by Oliveira et al. (2006) from ground-based K and L'-band images. Some stars are still in the accretion phase but the estimated accretion rates are low, with typical values $\dot{M}_{acc} < 10^{-8} M_{\odot} \text{ yr}^{-1}$ (Gatti et al. 2008).

X-ray observations of the σ Ori region have also been obtained with *XMM-Newton* and 174 X-ray sources were detected, 76 of which were identified with cluster members (Sanz-Forcada, Franciosini, & Pallavicini 2004; Franciosini, Pallavicini, & Sanz-Forcada 2006, hereafter FPS06). A 98 ksec *Chandra* HRC-I observation (ObsId 2560) has also been acquired, detecting more than 140 X-ray sources (Wolk et al. 2006) including faint X-ray emission from the infrared source IRS 1 located just 3."3 north of σ Ori AB (van Loon & Oliveira 2003; Caballero 2007b).

We present results of a sensitive *Chandra* X-ray observation of the σ Ori cluster obtained with the High Energy Transmission Grating (HETG) and the ACIS-S detector. This observation provides higher spatial resolution than the previous *XMM-Newton* observation, but over a smaller field-of-view. The spatial resolution acquired here is comparable to that of the *Chandra* HRC-I observation, but the HETG/ACIS-S combination provides spectral information whereas HRC-I does not. On the other hand, the HRC-I is more sensitive, covers a larger field-of-view, and gives superior image quality. Thus, the existing *Chandra* and *XMM-Newton* data sets are complementary.

Our primary objective was to obtain a high-resolution X-ray spectrum of σ Ori AB to test wind shock models of X-ray emission in massive stars. We focus on spectral properties of σ Ori AB but also analyze zeroth order CCD images, spectra, and light curves of 41 other X-ray sources near σ Ori AB, including the magnetic helium-strong B2Vpe star σ Ori E (HD

37479) and the unusual infrared source IRS1.

2. Chandra Observations and Data Reduction

The *Chandra* observation (ObsId 3738) began on 2003 August 12 at 20:59:02 UT and ended on August 13 at 23:29:25 UT, yielding 90,967 s of usable exposure. Pointing was centered near σ Ori AB (HD 37468) at nominal pointing coordinates (J2000.0) R.A. = $05^{\text{h}}38^{\text{m}}44.^{\text{s}}43$, decl. = $-02^{\circ}35'25.''9$. Grating spectra of σ Ori AB were obtained with the High-Energy Transmission Grating (HETG) using the ACIS-S detector in faint timed event mode with 3.2 s frame times.

The Level 1 events file provided by the *Chandra* X-ray Center (CXC) was processed using CIAO v. 3.0¹ using standard science threads. The CIAO processing applied calibration updates (CALDB v. 2.26), selected good event patterns, removed streak artifacts from CCD-8, determined zero-order source centroids, defined grating arm masks and extracted grating spectra, and created response matrix files (RMFs) and auxiliary response files (ARFs) for the extracted spectra. The spectral extraction provides separate dispersed spectra for the medium-energy grating (MEG) and high-energy grating (HEG). The HEG provides higher spectral resolution ($\Delta\lambda = 12 \text{ m}\text{\AA}$ FWHM, 1.2 - 15 \AA) than the MEG ($\Delta\lambda = 23 \text{ m}\text{\AA}$, 2.5 - 31 \AA) but the MEG gives a higher signal-to-noise ratio (S/N) in 1st order spectra for σ Ori AB. We focus here on the higher S/N data obtained in MEG 1st order spectra, combining the +1 and -1 orders for spectral analysis.

Additionally, we used the CIAO *wavdetect* tool to identify X-ray sources on the primary ACIS-S3 chip (CCD-7) which covers a $\approx 8.3' \times 8.3'$ region near the primary target σ Ori AB. We ran *wavdetect* on full-resolution (0.''49 pixels) images using events in the 0.5 - 7 keV range to reduce the background. The *wavdetect* threshold was set at *sigthresh* = 1.5×10^{-5} and scale sizes of 1,2,4,8, and 16 were used. We visually compared the *wavdetect* source list against the ACIS-S image and the archived HRC-I image to check for spurious and missed detections.

CIAO *psextract* was used to extract zero-order source and background spectra for brighter sources (>100 net counts). The nominal extraction radius used was $R_e = 4$ pixels (= 1.''97). Zero order light curves were also extracted for brighter sources using CIAO

¹Further information on *Chandra* Interactive Analysis of Observations (CIAO) software can be found at <http://asc.harvard.edu/ciao>.

tools. Spectral and timing analysis were undertaken with the HEASOFT *Xanadu*² software package including XSPEC v. 12.3.0. We also used a modified version of the ISIS v. 1.4.8³ spectral analysis package to complement the XSPEC analysis. The ISIS implementation allows the flux ratios of the resonance (r), intercombination (i), and forbidden (f) lines in He-like ions to be varied as free parameters when fitting grating spectra. This is an advantage for OB stars since their f/i line flux ratios can be affected by the strong UV radiation field. The modified ISIS package is discussed in more detail by Cohen et al. (2008).

3. X-ray Source Identification and Properties

3.1. Source Identification

Our analysis of zero-order data focuses on sources detected on the ACIS-S3 chip (CCD7) which contains the primary target σ Ori AB. Sources detected on the other chips in the ACIS-S array lie far off-axis and are heavily vignetted and will not be discussed here. Figure 1 shows the positions of the 42 sources detected on ACIS-S3 and their properties are summarized in Table 2. All of the sources in Table 2 are also visible in the archived HRC-I image (obsId 2560).

Figure 2 is a zoomed view of the ACIS-S3 image in the vicinity of σ Ori AB, the brightest X-ray source on ACIS-S3. The infrared source IRS1 lying 3."3 north of σ Ori AB is also detected (CXO 19). Other noteworthy detections are the magnetic B2Vpe star σ Ori E (CXO 23; Sec. 3.7.2) and the B5V star HD 37525, the latter being a known binary (Sec. 3.7.3). Interestingly, we do not detect the B2V star σ Ori D even though its spectral type is the same as σ Ori E, a clue that σ Ori E is anomalously bright in X-rays for its spectral type. We do note however that an X-ray source at or near the position of σ Ori D is visible in the more sensitive HRC-I image. The A-type star σ Ori C was not detected.

All but five of the X-ray sources in Table 2 have optical or near-IR counterparts as determined from a search of the HEASARC object catalogs⁴ using a 2" search radius. As Table 2 shows, the offsets between the X-ray and IR/optical positions are in all cases $<1''$ and in most cases $<0.''5$. Interestingly, no IR counterpart was found for CXO 8, which is one of the brighter X-ray sources. However, a faint $V = 20.88$ mag optical source was found

²<http://heasarc.gsfc.nasa.gov/docs/xanadu/xanadu.html>.

³<http://space.mit.edu/csc/isis/>

⁴<http://heasarc.gsfc.nasa.gov/docs/archive.html>

in Mayne et al. (2007) at an offset of 0."18 from the X-ray position. The X-ray source has an unusually hard spectrum (discussed below) and is variable. Further deep optical and infrared observations would be useful to elucidate its nature.

3.2. Faint Detections and Detection Limit

The faintest ACIS-S X-ray detection (CXO 32) has 5 ± 2 counts and is confirmed in the HRC-I image. Assuming a slightly more conservative 7 count detection threshold, the corresponding X-ray luminosity threshold determined from PIMMS⁵ at a cluster distance $d \approx 390$ pc is $\log L_x = 28.81$ ergs s^{-1} (0.5 - 7 keV). Here we have assumed a typical late-type pre-main-sequence star modeled as an isothermal X-ray source with a Raymond-Smith plasma at $kT = 2$ keV and an absorption column density $N_H = 3 \times 10^{20}$ cm^{-2} ($E(B-V) \approx 0.05$; Gorenstein 1975 conversion).

At a luminosity threshold $\log L_x = 28.81$ ergs s^{-1} we would expect to detect X-ray emission from pre-main sequence stars in Orion down to masses of $\sim 0.2 - 0.3 M_\odot$, based on previous deep *Chandra* Orion observations (Figs. 3 and 7 of Preibisch et al. 2005). A comparison of the X-ray detections in Table 2 with the optical catalog of Sherry, Walter, & Wolk (2004, = S04) confirms this. Two low-mass detections are S04 15 = CXO 17 and S04 18 = CXO 31, both of which have high cluster membership probability (92% - 93%). Their mass estimates from S04 are $0.22 M_\odot$ (S04 15) and $0.18 M_\odot$ (S04 18) and their respective V - R_c colors imply equivalent main-sequence spectral types of $\sim M4V - M5V$ (Kenyon & Hartmann 1995). Also noteworthy is *Chandra* source CXO 22, which was classified as M5 by FPS06 but was listed in their Table A.2 (object name B3.01-67) as undetected by *XMM-Newton*.

3.3. Hardness

The typical mean photon energy (Table 2) of detected sources is $\langle E \rangle = 1.83$ keV and the distribution of $\langle E \rangle$ values is shown in Figure 3. The brightest X-ray source σ Ori AB also has the lowest mean energy $\langle E \rangle = 0.86$ keV. The hardest emission is from the very faint source CXO 32 with $\langle E \rangle = 4.06$ keV, for which no optical or IR counterpart was found. These properties suggest that it may be an extragalactic background source.

⁵For information on PIMMS (Portable Interactive Multi-Mission Simulator) see <http://asc.harvard.edu/ciao/ahelp/pimms.html>.

3.4. Variability

Nine sources have high probability of variability $P_{var} \geq 0.95$ based on the Kolmogorov-Smirnov (KS) test (Press et al. 1992) using unbinned photon arrival times, as noted in column 4 of Table 2. The X-ray light curve of σ Ori AB (Fig. 4) shows no evidence of large-amplitude variability. A KS test on unbinned events gives a probability of constant count rate $P_{const} = 0.065$, slightly above the limit $P_{const} \leq 0.05$ that we adopt for variability. A χ^2 test on the light curve binned at 4000 s intervals (≈ 108 counts/bin) gives $P_{const} > 0.999$. Thus, we find no evidence for significant X-ray variability in σ Ori AB.

The magnetic B2Vpe star σ Ori E is variable (Fig. 5; see also Sec. 3.7.2). However, no large flares were detected, in contrast to the large outbursts seen in the *XMM-Newton* observation (Sanz-Forcada et al. 2004) and in the *Chandra* HRC-I exposure. Slow low-amplitude X-ray variability is seen in the unusual hard source CXO 8 (Fig. 6). X-ray flares are clearly visible in CXO 9 (Fig. 7) and CXO 25 (Fig. 8). The counterpart of CXO 9 has been classified as K8 and has properties of a weak-lined TTS (Zapatero Osorio et al. 2002). CXO 25 is associated with a M4 star that has a near-IR excess (Oliveira et al. 2006) indicative of a residual disk or envelope. The second brightest X-ray source in Table 2 (CXO 37) showed a slow decline in count rate by a factor of two during the observation, but no large flares.

3.5. Near-IR Colors

Figure 9 shows J- K_s colors of those X-ray detections with 2MASS identifications. IRS1 was not resolved from σ Ori AB by 2MASS and no published JHK magnitudes are available. Most of the sources cluster in the range $0.7 \leq J-K_s \leq 1.3$, typical of early K to late M dwarfs or giants (Bessell & Brett 1988). The three massive stars σ Ori AB, σ Ori E, and the B5V star HD 37525 are clearly separated in color-magnitude space by their smaller J- K_s and K_s values. An interesting outlier is the faint hard variable X-ray source CXO 12 which has a large value $J-K_s = 2.33$ and is the faintest near-IR identification with $K_s = 14.04$. It is associated with a faint $V = 18.8$ mag optical source (Mayne et al. 2007).

Figure 10 is a color-color diagram based on 2MASS JHK_s photometry of X-ray detections with 2MASS identifications. Excluding the three known high-mass stars, nineteen of the X-ray sources in Figure 10 have assigned spectral types (FPS06) and all of these are K or M stars. This substantiates the above conclusion that most of the low-mass X-ray detections are K or M stars. Of the nineteen X-ray sources with spectral types, slightly more than half lie to the right of their respective K0V or M0V normal-reddening lines. Based on this

limited information, we conclude that about half of the low-mass detections are normally reddened and half are moderately reddened. A clear exception is CXO 12 (noted above) which is heavily-reddened compared to the other X-ray sources.

3.6. CCD Spectra

We have fitted the zero-order CCD spectra of brighter sources (≥ 100 counts) with one-temperature (1T) or two-temperature (2T) *apec* solar-abundance optically thin plasma models (Smith et al. 2001) in XSPEC, as summarized in Table 3. We have also fitted the spectrum of the high-interest object IRS1 (CXO 19), but the fit is not well-constrained because this source is faint (43 counts). Photon pileup is low ($\approx 5\%$) in the zero-order spectrum of σ Ori AB (negligible in first order) and zero-order pileup is negligible ($< 1.7\%$) in all the other sources.

In all but a few sources there were insufficient counts to constrain both the temperature and absorption column density, so we held the absorption fixed at $N_{\text{H}} = 3 \times 10^{20} \text{ cm}^{-2}$, consistent with $E(B-V) \approx 0.05$ mag for the σ Ori region. The best-fit value of N_{H} was within a factor of ≈ 2 of the above value for the brighter sources where N_{H} was allowed to vary during the fit.

Two-temperature models provide an acceptable approximation to the spectra in most cases. With the notable exception of σ Ori AB (discussed below), the derived temperatures from 2T models are typical of magnetically-active pre-main sequence stars in the Orion region (Preibisch & Feigelson 2005), showing both a cool component ($kT_1 < 1 \text{ keV}$) and hotter plasma in the range $kT_2 \approx 2 - 3 \text{ keV}$.

3.7. Comments on Specific Stars

3.7.1. HD 37468 (σ Ori AB)

Fits of the CCD spectrum of σ Ori AB excluded events with energies below 0.5 keV to avoid possible contamination from optical light leaks ⁶. A simple 1T *apec* optically thin

⁶The ACIS CCDs are sensitive at optical frequencies but most optical light is diffracted away from the CCDs by the optical blocking filter. Also, the optical sensitivity is further reduced when the MEG/HEG gratings are in place. Further details can be found at http://www.astro.psu.edu/xray/docs/cal_report/node188.html.

plasma model (1T *apec*) was not acceptable. But, a 2T *apec* model does give an acceptable fit (Fig. 11) with two cool components at $kT_1 = 0.21$ keV and $kT_2 = 0.47$ keV whose emission-measure weighted average is $kT = 0.3$ keV. A fit with the differential emission measure model *c6pmekl* in XSPEC using solar abundances gives good results ($\chi^2/\text{dof} = 43.4/44$) and shows a single broad peak in the emission measure between 0.2 - 0.3 keV with significant emission measure over the 0.15 - 0.45 keV range (Fig. 12). Thus, the 2T model is probably an approximation to this broad cool emission measure distribution. The spectrum of σ Ori AB is clearly dominated by cool plasma, consistent with expectations for radiative wind shocks.

As noted above, *Chandra* does not spatially resolve the A and B components. Thus, our observation does not exclude the possibility that the X-ray emission is the superposition of soft emission from the O9.5V primary and the B0.5V secondary. Soft X-ray emission from some B-type stars in Orion has previously been reported, including the B0.5 star θ^1 Ori D (Stelzer et al. 2005).

3.7.2. HD 37479 (σ Ori E)

The helium-strong star σ Ori E has been extensively studied and is known to exhibit optical, UV, and radio modulations at a period $P = 1.1908$ days (Reiners et al. 2000), which has been interpreted as the stellar rotation period. A strong magnetic field that varies from -2.2 to $+2.8$ kG at the 1.19 day period was detected by Landstreet & Borra (1978) and discussed further by Borra & Landstreet (1979). A distance of 640 pc was obtained by Hunger, Heber, & Groote (1989) which, if correct, would place it behind the σ Ori cluster.

An X-ray flare detected by *ROSAT* was reported by Groote & Schmitt (2004), who concluded that the flare likely occurred on the magnetic B star and not on a hypothesized late-type companion. A large X-ray flare whose rise and decay spanned at least ≈ 8 hours was also detected by *XMM* (Sanz-Forcada et al. 2004). The X-ray flare CCD spectrum recorded by the PN camera showed fluorescent Fe emission at ≈ 6.4 keV, a signature of cool neutral or near-neutral material near the star that was irradiated by hard X-rays during the flare. Sanz-Forcada et al. argued that an unseen low-mass companion was likely responsible for the flare. A large flare is also visible in the archived *Chandra* HRC-I data.

The *Chandra* ACIS zero order light curve (Fig. 5) is clearly variable but no large-amplitude flares were detected. A KS test gives a probability of constant count rate $P_{const} = 0.014$. Low-level modulation may be present in the ACIS light curve, as shown in Figure 5. However, the *Chandra* observation spanned only 88% of the 1.19 day rotation period and

additional time monitoring over more than one period would be needed to substantiate any periodic X-ray modulation.

The *Chandra* ACIS spectrum of σ Ori E (Fig. 13) is definitely harder than that of σ Ori AB, as anticipated from their respective mean photon energies (Table 2). However, the ACIS spectrum is not as hard as seen by *XMM* during the flare state and we do not detect the fluorescent Fe line at 6.4 keV. A 2T *apec* model of the ACIS spectrum gives a marginally acceptable fit with a high-temperature component at $kT_2 = 2.4$ keV, which is typical of magnetically-active stars. The fit can be improved by using a 3T model and allowing N_H to vary (Table 3 Notes), and this fit is overlaid in Figure 13. The 3T model gives a temperature $kT_3 = 2.6$ [2.1 - 3.3; 90% confidence] keV for the hot component, and the inferred value of N_H is consistent with $E(B-V) = 0.05$ (or possibly larger) estimated for this star by Hunger et al. (1989).

The stellar luminosity from the blackbody relation is $L_* = 2.48 \times 10^{37}$ ergs s^{-1} , or $\log(L_*/L_\odot) = 3.81$, where we have assumed $T_{eff} = 22,500$ K and $R_* = 5.3 R_\odot$ from Hunger et al. (1989). The unabsorbed flux from the 3T model gives an X-ray luminosity L_x (0.5 - 7 keV) $= 2.88 \times 10^{25} d_{pc}^2$, where d_{pc} is the distance in parsecs. Adopting $d = 640$ pc (Hunger et al. 1989) gives $\log(L_x/L_*) = -6.32$. This ratio is much higher than usually found for B2V stars, for which a catalog of *ROSAT* detections gives typical values $\log(L_x/L_*) \approx -7.2$ to -6.8 (Berghöfer et al. 1996). In fact, these typical values are too large since the *ROSAT* All Sky Survey (RASS) was based on short exposures and thus selected in favor of the detection of X-ray bright B2V stars. A ratio $\log(L_x/L_*) \approx -8$. may actually be more representative (Cohen, Cassinelli, & MacFarlane 1997). This strengthens the conclusion that the value of L_x/L_* for σ Ori E at $d = 640$ pc is anomalously large for a B2V star. This is a clue that the star lies closer and may be in the σ Ori cluster, not behind it.

If σ Ori E lies in the cluster at $d \sim 390$ pc, then $\log(L_x/L_*) = -6.75$. This is in better agreement with other B2V stars, but still at the high end of the range. The high L_x/L_* ratio obtained even at the nominal cluster distance, along with persistent flaring, leave open the possibility that a late-type companion may be contributing to the X-ray emission of σ Ori E. However, there have been no reports of the detection of a companion so far.

The rather high plasma temperature for this star and its X-ray variability are not consistent with radiative wind shock predictions. The detection of a strong magnetic field gives reason to believe that the magnetically-confined wind shock (MCWS) picture may be relevant. This model is capable of producing higher plasma temperatures than the conventional radiative wind shock scenario and was originally formulated to explain hot plasma in stars with strong \sim kG magnetic fields such as the Ap star IQ Aur (Babel & Montmerle 1997a = BM97a). It has also been invoked to explain hard rotationally-modulated X-ray emission in

the young magnetic O star θ^1 Ori C (Babel & Montmerle 1997b; Gagné et al. 2005; Schulz et al. 2000). The good agreement between model predictions and observed X-ray parameters for θ^1 Ori C found by Gagné et al. provides solid support for the MCWS interpretation.

In the MCWS picture, a strong surface magnetic field can channel the wind flow into two oppositely directed streams from each hemisphere, which collide near the magnetic equator and liberate their kinetic energy in shock-heated plasma. The degree to which the wind is confined by the magnetic field is expressed in terms of the confinement parameter $\eta = B_{eq}^2 R_*^2 / \dot{M} v_\infty$ where B_{eq} is the equatorial magnetic field strength (ud-Doula & Owocki 2002). For $B \sim 2$ kG and plausible mass-loss parameters (Groote & Hunger 1997), one obtains $\eta \gg 1$ for σ Ori E. That is, the wind is strongly confined by the magnetic field.

Building on earlier work, Townsend, Owocki, & Groote (2005) extended the MCWS idea into a rigidly rotating magnetosphere model. They showed that by allowing for the center of a dipole magnetic field to be displaced away from the center of the star, many aspects of the periodic behavior of σ Ori E could be explained. This work has now been expanded into a rigid field hydrodynamics (RFHD) approach by Townsend, Owocki, & ud-Doula (2007). The RFHD approach is relevant to stars with strong magnetic fields such as σ Ori E where the wind has little effect on the field lines.

Numerical RFHD simulations of the X-ray emission of a generic star with properties similar to σ Ori E by Townsend et al. (2007) predict hot plasma with an emission measure distribution peaking near $kT \approx 3.5$ keV. This is somewhat hotter than we infer from our best-fit 3T model, which gives $kT_3 = 2.6$ [2.1 - 3.3; 90% conf.] keV. However, as Townsend et al. (2007) have noted, the higher temperature in the RFHD model could be a consequence of neglecting thermal conduction effects and uncertainties in the mass loss parameters. Future refinements of the RFHD model tailored specifically to σ Ori E will address these temperature differences and also have the potential to provide theoretical estimates of the X-ray luminosity and X-ray absorption that can be directly compared with observations.

3.7.3. HD 37525

This star is classified as B5V and has a known companion at a separation of $0.''45 \pm 0.''04$ (Caballero 2005). The *Chandra* ACIS-S spatial resolution is not sufficient to distinguish between the primary and the companion. But, if the companion is a pre-main sequence star (Caballero 2005), then it likely contributes to the X-ray emission.

3.7.4. σ Ori IRS1

IRS1 was discovered in sub-arcsecond mid-IR observations of σ Orionis with the ESO 3.6 m telescope by van Loon & Oliveira (2003). It shows a clear near to mid-IR excess indicative of a disk. The mid-IR emission displays fan-shaped morphology, giving confidence that IRS1 is physically associated with σ Ori AB and is being influenced by the strong OB system radiation field.

IRS1 was serendipitously detected in earlier *VLA* radio observations of σ Ori AB by Drake (1990). The radio source discovered by Drake lies $2.6''$ north and $0.45''$ east of the Simbad optical position of σ Ori AB. Thus, the radio source lies much closer to IRS1 than σ Ori AB, and the radio position is offset slightly from IRS1 toward σ Ori AB. Adopting the wind parameters for σ Ori AB in Table 1, the predicted 6 cm radio flux density for free-free emission from a spherical fully-ionized wind is $S_{4.86GHz} = 0.1$ mJy (eq. [7] of Skinner, Brown, & Stewart 1993). This is consistent with the upper limit on the emission from σ Ori AB from the *VLA* observations $S_{4.86GHz} \leq 0.3$ mJy (S. Drake, private communication).

Chandra's high angular resolution clearly separates the faint X-ray source IRS1 (CXO 20) from σ Ori AB (Fig. 2). Only 43 net counts were detected from IRS1, but this provides enough information to undertake a rudimentary spectral analysis. The CCD spectrum (Fig. 14) is absorbed below ≈ 0.7 keV and peaks at $kT \approx 1$ keV. Spectral fits imply hotter plasma at $kT > 1$ keV (Table 3). The unabsorbed X-ray luminosity at an assumed distance of 352 pc is $\log L_x (0.5 - 7 \text{ keV}) = 29.53 \text{ ergs s}^{-1}$. The detection of variable X-ray emission from IRS1 at a plasma temperature of $kT \approx 1$ keV (and perhaps higher) demonstrates that the infrared source detected by van Loon & Oliveira harbors a magnetically-active young star.

The *Chandra* COUP study has shown that the X-ray luminosity of optically-revealed pre-main sequence (PMS) stars in the Orion nebula correlates with mass, albeit with large scatter (Preibisch et al. 2005). Assuming a similar correlation for the σ Ori cluster, the above L_x along with the mid-IR data would imply that IRS1 is likely a T Tauri star with a mass of a few tenths of a solar mass whose disk/envelope is being photo-evaporated in the harsh UV environment of σ Ori AB.

3.7.5. Source CXO 8 (*J053835.21–023438.1*)

A thermal plasma model requires a very high temperature for the variable source CXO 8, but a simple absorbed power-law model also gives an acceptable fit (Table 3). We find no counterpart in HEASARC extragalactic catalogs but the X-ray source lies at a small offset from a faint $V = 20.88$ mag optical source (Mayne et al. 2007).

4. Grating Spectrum of σ Ori AB

4.1. General Properties

Figure 15 shows the first-order MEG1 spectrum of σ Ori AB with prominent lines identified. Line properties are summarized in Table 4.

In order to test the feasibility of various emission models (Sec. 5.), we need information on X-ray temperature, line widths, line centroid shifts (if any), and flux ratios of specific lines. Information on line shape is also important, since radiative wind shock models predict line asymmetries for optically thick winds. But at the signal-to-noise ratio of the MEG1 spectrum, the lines can be acceptably fitted with Gaussians and we do not find any conclusive evidence of line asymmetries.

The spectrum is clearly dominated by lines from relatively cool plasma, with the coolest lines being the O VII He-like triplet r and i lines and the O VII line at 18.627 \AA ($\log T_{max} = 6.3 \text{ K}$). The highest temperature and shortest wavelength line detected was Si XIII ($\lambda_{lab} = 6.6479 \text{ \AA}$; $\log T_{max} = 7.0 \text{ K}$).

4.2. Line Widths

Line fluxes and widths were based on fits with a weak power-law component plus a Gaussian profile convolved with the instrumental response. The weak power-law component accounts for faint emission outside the line, due either to true continuum or a pseudo-continuum arising from many faint unresolved lines.

The strongest lines based on observed line flux are O VIII ($\lambda_{lab} = 18.967 \text{ \AA}$) and the O VII intercombination line ($\lambda_{lab} = 21.804 \text{ \AA}$). In general, all lines for which widths could be reliably measured are moderately broadened in excess of thermal (Doppler) widths, the latter being no greater than $\sim 60 \text{ km s}^{-1}$ for the detected ions at a temperature $T \sim 3.5 \text{ MK}$.

Gaussian fits of nine prominent lines give a mean half-width at half-maximum $\overline{\text{HWHM}} = 264 \pm 80 (1\sigma) \text{ km s}^{-1}$. Spectral fits with ISIS give nearly identical results. Taking the uncertainties of the line width measurements into account, there is no clear dependence of line width on wavelength or maximum line power temperatures T_{max} (Figs. 16 - 17).

The mean HWHM for σ Ori AB is much less than observed for O supergiants (Figure 6 of Cohen et al. 2003), slightly less than for the O9.5 II star δ Ori (HWHM = 430 km s^{-1} ; Miller et al. 2002), very similar to that of the B0.2V star τ Sco (Cohen et al. 2003), but slightly larger than found for the B0.5 III star β Cru (HWHM $\approx 150 \text{ km s}^{-1}$; Cohen et al.

2008). Although there is considerable scatter in the line widths for any particular star and the sample is still small, these results suggest tentatively that there is a trend for broader lines in O stars with stronger winds versus B stars with weaker winds. The mean HWHM value for σ Ori AB is well below the terminal wind speed $v_\infty \approx 1060 \text{ km s}^{-1}$ (Howarth and Prinja 1989). Expressed as a ratio, the value from individual line fits gives $\overline{\text{HWHM}}/v_\infty = 0.22 - 0.25$. These ratios are comparable to the value 0.22 found for δ Ori (Miller et al. 2002).

4.3. Line Centroids

Gaussian line centroids were measured for 13 stronger lines. In all cases the centroids lie within 7 mÅ of the laboratory values and for eight lines the offsets are ≤ 3 mÅ, as shown in Figure 18. These offsets are well within the ± 11 mÅ absolute wavelength calibration accuracy of MEG1⁷. Both positive and negative offsets were found with ten lines blueshifted and three redshifted. The mean centroid offset was -1.6 ± 3.5 ($\pm 1\sigma$) mÅ. In only two cases does λ_{lab} lie outside the $\pm 1\sigma$ uncertainty interval of the measured centroid. The centroid measurements of these two lines are uncertain due to close blends (Ne X 12.1321/12.1375 Å) and possible contamination by weak nearby Fe lines (Ne IX 13.553 Å).

4.4. Helium-like Ions

He-like triplets show strong resonance (r) and intercombination (i) lines, but the forbidden (f) lines are very faint and formally undetected. The resonance and intercombination lines were detected in the Mg XI (Fig. 19), Ne IX (Fig. 20), and O VII (Fig. 21) He-like triplets. The Si XIII resonance line was detected but the emission in the triplet is so faint that no reliable diagnostic information can be obtained apart from an estimate of the resonance line flux. The strong i lines and faint or absent f lines are a clear indication that the f and i line fluxes are being affected by the strong UV radiation field of σ Ori A ($T_{eff} = 33,000 \text{ K}$; Howarth & Prinja 1989).

In general, the flux ratio $R = f/i$ is sensitive to both electron density n and the UV radiation field (Gabriel & Jordan 1969). If ϕ is the photoexcitation rate from the 3S_1 level to the $^3P_{2,1}$ levels, then $R = R_0/[1 + (\phi/\phi_c) + (n/n_c)]$, where ϕ_c and n_c are the critical photoexcitation rate and critical density (Blumenthal, Drake, & Tucker 1972). If photoexcitation is

⁷Chandra Proposer’s Observatory Guide: <http://asc.harvard.edu/proposer/POG/> .

negligible then $R \rightarrow R_0$ in the low-density limit ($n \ll n_c$).

In hot stars where the UV excitation is important, the ratio R is not a reliable density diagnostic but it can be used to estimate the line formation radius from the star. The most stringent limit from the MEG spectrum of σ Ori AB is obtained from Mg XI. We have used a solar abundance TLUSTY model atmosphere (Lanz & Hubeny 2007) with $T_{eff} = 32,500$ and $\log g = 4.0$, along with the formalism in Blumenthal et al. (1972) and Leutenegger et al. (2006), taking an average of the photospheric fluxes of the two $^3S - ^3P_{1,2}$ transitions (997.5 Å and 1034.3 Å for Mg XI). We have averaged these fluxes over ≈ 3 Å blueward of these wavelengths to account for the Doppler shift in the wind (Leutenegger et al. 2006). We find an expression for the ratio $R(r) = f/i$ as a function of the distance r from the center of the star, which takes into account the dilution factor $W(r)$ and is plotted in Figure 22.

For Mg XI our spectral fits give a 90% confidence upper limit $R = f/i \leq 0.17$ (Table 5). As can be seen in Figure 22, this upper limit implies a small line formation radius $r \leq 1.8 R_*$. A similar analysis for Ne IX gives $R \leq 0.15$ and a formation radius $r \leq 4.4 R_*$. The O VII triplet does not provide a useful constraint on the line formation radius. Using the adopted mass-loss parameters in Table 1 and an estimated wind X-ray opacity $\kappa_w \approx 80 \text{ cm}^2 \text{ g}^{-1}$ near $E \approx 1 \text{ keV}$ (Waldron et al. 1998; Cohen et al. 1996; Ignace, Oskinova, & Foullon 2000), the wind is expected to be optically thin at $E \approx 1 \text{ keV}$ down to the stellar surface. In addition, our modeling of the Fe XVII line (15.014 Å) confirms that the wind optical depth is consistent with zero. Thus, X-rays formed at the small radii given above could escape through the wind.

4.5. Abundances

We have simultaneously fitted the zero-order spectrum and the MEG1 and HEG1 first order spectra of σ Ori AB to search for significant deviations from solar abundances. These fits were conducted using an absorbed 2T *vapex* model with a modified version of ISIS (Cohen et al. 2008) that allows the R and G ratios of He-like triplets to be fitted as free parameters. We allowed the abundances elements with prominent lines in the spectrum to vary, namely O, Ne, Mg, Si, and Fe. We found no significant deviations from solar abundances. The largest deviation found was for magnesium, which gave a best-fit abundance $\text{Mg} = 0.78 [0.62 - 1.08; 90\% \text{ conf.}] \times \text{solar}$.

4.6. Summary of Grating Spectra Results

In summary, the key properties determined from the spectral analysis of σ Ori AB are: (i) dominant cool plasma ($kT \approx 0.3$ keV), (ii) moderate line broadening (HWHM ≈ 264 km s^{-1}) that is a factor of ~ 4 below the terminal wind speed of σ Ori, (iii) no significant mean line centroid shifts relative to laboratory values, (iv) strong resonance and intercombination lines and very faint (formally undetected) forbidden lines with low f/i flux ratios, indicative of strong UV field excitation effects, and (v) Mg XI line formation within a few radii of the star ($r \lesssim 1.8 R_*$).

5. Interpretation of the X-ray Emission from σ Ori AB

5.1. Radiative Wind Shocks

The temperature of the cool plasma that dominates the X-ray emission of σ Ori AB is in good agreement with model predictions for shocks distributed in a radiatively-driven stellar wind. Numerical radiation hydrodynamics simulations of shocks in radiatively-driven winds give typical shock jumps $\Delta V = 500 - 1000$ km s^{-1} and post-shock temperatures in the range $\sim 1 - 10$ MK (Owocki, Castor, & Rybicki 1988). This range can easily accommodate σ Ori AB, whose emission-measure weighted temperature from the best-fit 2T *apec* model is $T \sim 3.5$ MK.

The predicted post-shock X-ray temperature corresponding to a shock jump velocity ΔV is $T_x = 1.4 \times 10^5 (\Delta V/100 \text{ km } s^{-1})^2$ K (Krolik & Raymond 1985). For σ Ori AB we have $T \sim 3.5 \times 10^6$ K ($kT = 0.3$ keV) so the required shock jump is $\Delta V \approx 500$ km s^{-1} , or about half the terminal wind speed.

Also, the emission measure (EM) in the wind is sufficient to account for the observed X-ray emission measure. The wind emission measure outside a given radius R_o is $EM_{wind}(r > R_o) = \int_{R_o}^{\infty} n_e n_H 4\pi r^2 dr$, where n_e and n_H are the electron and hydrogen number densities. Using the mass loss parameters for σ Ori AB in Table 1 and assuming a solar-abundance constant-velocity wind with $v(r) = v_{\infty}$ we have $EM_{wind}(r > R_o) = 5.5 \times 10^{55}/R_o$ cm^{-3} , where R_o is in units of $R_* = 9 R_{\odot}$. By comparison, the total X-ray emission measure determined from the best-fit 2T *apec* model is $EM_X = 1.8 \times 10^{54}$ cm^{-3} . To compute this value, we have converted the normalization factors (*norm*) for both temperature components in Table 3 to equivalent emission measures and summed them, using the conversion $EM = 10^{14} 4\pi d_{cm}^2 norm$, where d_{cm} is the stellar distance in cm. Adopting $R_o = 1.5$ as a representative example gives an inferred ratio of X-ray EM to wind EM of $\approx 5\%$. Thus, the emission measure of the X-ray

emitting plasma relative to that of the wind is low.

The grating spectra provide clues that a significant fraction of the X-ray emission originates close to the star in the region where the wind is still accelerating. The relatively narrow lines and absence of any significant centroid shifts are good evidence that the bulk of the X-ray plasma is slowly moving and does not form at large radii where the wind has reached terminal speed. Also, the very weak (formally undetected) forbidden lines in He-like triplets imply line formation close to the star. As already noted, the most stringent constraint on the location of the X-ray emitting plasma comes from the Mg XI triplet, for which we infer an upper limit on the line formation radius $r < 1.8 R_*$ (Fig. 22). Assuming a standard wind acceleration law $v(r) = v_\infty[1 - (R_*/r)]^\beta$ and $v_\infty = 1060 \text{ km s}^{-1}$ (Table 1), the above radius is within the acceleration zone for typical hot star wind values $\beta \approx 0.5 - 1.0$. A recent analysis of He-like triplet line ratios in O stars by Leutenegger et al. (2006) concludes that minimum line formation radii are typically $1.25 < r/R_* < 1.67$ and that these small radii do not preclude the formation of strong shocks.

One issue that could pose difficulties for the radiative wind shock interpretation for σ Ori AB and some other late O and early B stars is the narrow line widths. The observed X-ray line widths are sensitive to the velocity of the shocked wind, which increases with radial distance from the star until terminal speed is reached. To explain the relatively narrow lines observed for σ Ori AB, the shocked wind material must be moving quite slowly. For a $\beta = 1$ wind velocity law, the wind would achieve a velocity equivalent to HWHM $\sim 260 \text{ km s}^{-1}$ ($\sim 0.25v_\infty$) at $r \approx 1.3 R_*$. This suggests that the shocks form rather close to the star, which would be consistent with the upper limit on line formation radius inferred from the Mg XI f/i ratio (Table 5). By comparison, numerical simulations of the line-driven instability mechanism (e.g. Feldmeier, Puls, & Pauldrach 1997; Runacres & Owocki 2002), tend to show onset radii of about $1.5 R_*$ and velocities of shock-heated material that are an appreciable fraction of v_∞ . The line widths predicted by numerical simulations are sensitive to assumptions about wind properties and the wind velocity profile close to the star, which are uncertain for σ Ori AB and OB stars in general. It remains to be seen whether future simulations can reproduce the rather narrow lines in the framework of the line-driven instability mechanism. The issues of line widths and profiles in non-magnetic OB stars will be discussed in more detail in a future paper (D. Cohen et al., in preparation).

5.2. Magnetically-Confined Wind Shocks

As already mentioned in the discussion of σ Ori E (Sec. 3.7.2), a sufficiently strong surface magnetic field can channel the wind of a hot star into two streams, producing X-ray

emission from a magnetically-confined wind shock near the magnetic equator. There have been no reports of a magnetic field detection on σ Ori AB to date but since this star is young and its age is still rather uncertain (Table 1 of Caballero 2007), it might still retain a weak fossil magnetic field. We thus briefly consider the MCWS mechanism.

Using the relation for the wind confinement parameter η (Sec. 3.7.2) and the adopted stellar parameters for σ Ori A (Table 1), the field strength for critical confinement ($\eta = 1$) is $B_{eq} \approx 70$ G. Thus, even a relatively weak field could perturb the wind of σ Ori A but a field of this strength would be difficult to detect in a hot star.

Analytic expressions for the X-ray temperature and luminosity of a magnetically-confined wind shock were derived by BM97a. The predicted temperature at the shock front is $T_{shock} = 1.13 \times 10^5 v_{100}^2$ K, where v_{100} is the pre-shock wind speed in units of 100 km s^{-1} . In order to reconcile the MCWS picture with the relatively cool emission at $T \sim 3.5$ MK observed for σ Ori AB, one would need to postulate a pre-shock wind speed of $v \sim 550 \text{ km s}^{-1}$. This is about half the terminal wind speed and would require that the closed field lines exist only in the wind acceleration zone near the star. Intuitively, this is what one would expect in the weak confinement regime.

The predicted X-ray luminosity from a magnetically-confined wind shock in the BM97a model is $L_x \approx 2.6 \times 10^{30} B_{kG}^{0.4} \xi \text{ ergs s}^{-1}$. Here, B_{kG} is the field strength in kG and ξ is a free parameter of the theory that depends on \dot{M} and v_∞ . For critical confinement ($B \sim 70$ G.), this relation requires $\xi \sim 35$ to account for the observed L_x (Table 1). This value of ξ is within the (broad) range allowed by the theory and the adopted mass-loss parameters of σ Ori AB.

Based on the above comparisons, we conclude that the MCWS model could plausibly account for the observed X-ray properties of σ Ori AB if the magnetic field is weak and only able to close the field lines near the star. Detailed MCWS simulations would be needed to test this idea. The justification for invoking the MCWS model is not strong in the absence of a magnetic field detection or any documented $H\alpha$ or UV wind line modulation.

5.3. Colliding Wind Shocks

The presence of a B0.5V companion at a separation of $0.''25$ from σ Ori A raises the possibility that X-rays could be produced in a colliding wind shock region between the two stars. However, the predicted maximum X-ray temperature for a colliding wind shock is $kT_{cw} \approx 1.95 (v_{\perp,1000})^2 \text{ keV}$, where $v_{\perp,1000}$ is the velocity of the wind component perpendicular to the shock interface in units of 1000 km s^{-1} (Luo, McCray, & MacLow 1990). Setting v_{\perp}

equal to the terminal wind speed of σ Ori AB gives $kT_{cw} \approx 2.2$ keV, much higher than observed.

Furthermore, wind momentum balance considerations predict that the shock contact discontinuity along the line-of-centers between the binary components will lie at least $\sim 1000 R_{O-star}$ from σ Ori A. This equates to about half the distance between the A and B components. To arrive at this estimate, we have assumed that the winds have reached terminal speeds and have used eq. [1] of Stevens, Blondin, & Pollock (1992), along with the mass-loss parameters in Table 1 and the assumed B0.5V star wind parameters $\log \dot{M}_{B-star} \sim -7.4$ to -8.0 ($M_{\odot} \text{ yr}^{-1}$) and $v_{\infty, B-star} \sim 2000 \text{ km s}^{-1}$ (Abbott 1982; Cassinelli et al. 1994). X-ray formation at such large distances is ruled out by the weak or absent forbidden lines in He-like ions, which for Mg XI demonstrate that the bulk of the X-rays are formed within a few radii of the O star.

Based on the above estimates, a colliding wind origin for the X-rays seems very unlikely. But, before ruling out this mechanism it is important to note that there have been several reports that σ Ori A is itself a double-lined spectroscopic binary (e.g. Bolton 1974; Morrell & Levato 1991), which if true would make σ Ori AB a triple system. This has also been mentioned by Caballero (2008) as a possible means of bringing the distance of σ Ori AB into better agreement with that of the cluster.

If the A component is indeed a spectroscopic binary then the wind of the more massive primary could be shocking onto the companion. From above, the wind speed needed to produce the $kT \approx 0.3$ keV plasma detected by *Chandra* is $v_{wind} \approx 390 \text{ km s}^{-1}$. This would imply that the wind is shocking at sub-terminal speed. For a $\beta = 1$ velocity law, this speed could be achieved at $r \approx 1.6 R_*$, which is consistent with the upper limit $r \leq 1.8 R_*$ obtained from Mg XI line flux ratios (Sec. 4.4). Such a close colliding wind system might be similar to the spectroscopic O3 + O6V binary HD 150136, but perhaps with an early B star playing the role of the spectroscopic companion to σ Ori A (Caballero 2008). It is interesting (but perhaps coincidental) that HD 150136 also shows a soft X-ray spectrum with a characteristic temperature $kT \approx 0.3$ keV (Skinner et al. 2005), identical to that of σ Ori AB.

If σ Ori A does have a spectroscopic companion, then orbitally-modulated X-ray emission could be present if the X-rays form in a colliding wind shock. But, the presence of orbital X-ray modulation depends critically on the orbital eccentricity and inclination, for which no information is currently available. We see no evidence of X-ray modulation in the ~ 1 day *Chandra* light curve. More specific information on the properties of the putative spectroscopic companion and its orbit would be needed to make further comparisons between colliding wind shock theory and the X-ray data.

5.4. Coronal Models and Late-Type Companions

The existence of a thin X-ray emitting coronal zone at the base of the wind was invoked by Cassinelli & Olson (1979) to explain strong O VI, N V, and C IV lines in some OB supergiants and Of stars. Waldron & Cassinelli (2001) have also surmised that dense plasma confined in magnetic loops near the surface of the O9.7 Ib star ζ Ori could explain its broad symmetric unshifted emission lines. Such a picture strongly resembles coronal models in late-type stars.

But the coronal model has not gained wide acceptance due to the lack of a solid theoretical basis for explaining how strong outer convection zones would be produced in hot stars. Such convection zones are thought to be essential for generating self-sustained magnetic fields in the Sun and other late-type stars. Even so, the detection of strong \sim kG magnetic fields in some very young O-type stars such as θ^1 Ori C does justify a brief examination of the possibility of coronal emission, either from σ Ori AB or an unseen late-type companion.

Because of the young age of σ Ori AB (\sim 3 Myr), a coeval unseen late-type companion would likely be a T Tauri star and thus a potential X-ray emitter. However, adaptive optics H-band images with FWHM \approx 0."2 - 0."4 (Caballero 2005) have only detected IRS1, which at a separation of \approx 3" is also revealed by *Chandra*. The best adaptive optics resolution of FWHM \approx 0."2 probes down to a linear separation of \sim 70 AU, so any as yet undetected T Tauri star would presumably lie very close to σ Ori A.

Coronal X-ray emission would be expected to show narrow unresolved emission lines as seen in the late-type star Capella (Ness et al. 2003), in contrast to the moderately-broadened lines visible in the MEG spectrum. Also, most TTS in the deep Orion COUP survey show a hot X-ray component at $kT > 1$ keV (Preibisch et al. 2005) and no such component is detected here in the X-ray source associated with σ Ori AB. Impulsive X-ray flaring or moderate amplitude variability on short timescales is often (but not always) detected in TTS but no such variability has so far been detected in σ Ori AB. Thus, we find no strong reason to invoke a coronal interpretation for the X-ray emission of σ Ori AB.

6. Conclusions

The main conclusions of this study are the following:

1. *Chandra* detected 42 X-ray sources on the ACIS-S3 CCD in the central region of the σ Ori cluster. Three are known high-mass OB stars and the remainder have X-ray and near-IR properties consistent with normally-reddened or moderately-reddened

magnetically-active K or M stars. The X-ray source CXO 12 is an exception and is heavily-reddened as gauged by its *2MASS* colors.

2. The X-ray emission associated with IRS1 is variable and shows a high-temperature ($kT \gtrsim 1$ keV) component. Its X-ray properties and fan-shaped mid-IR morphology suggest that it is a low-mass magnetically-active T Tauri star whose disk/envelope is being photo-evaporated by σ Ori AB.
3. The X-ray emission of σ Ori E is variable and a hard component ($kT \approx 2.6$ keV) is detected, as typical of magnetically-active stars. Its ratio L_x/L_* is unusually high for a B2V star assuming the nominal distance of 640 pc, suggesting that it could lie closer. Numerical magnetosphere models based on the magnetically confined wind picture predict hot plasma at temperatures similar to (but slightly higher than) observed and can also explain many aspects of the variability of this star (Townsend et al. 2005, 2007). Future numerical models offer the potential to provide estimates of X-ray luminosity and X-ray absorption that can be compared with observations.
4. The X-ray emission of the OB binary system σ Ori AB is exceptional, being the most luminous X-ray source in the field and the softest. Its low X-ray temperature ($kT \approx 0.3$ keV) and moderately-broadened emission lines ($\text{HWHM} \approx 264$ km s⁻¹) clearly argue against a coronal interpretation and point to a shock origin. Overall, its X-ray properties are quite similar to other late O and early B stars for which X-ray grating spectra show relatively cool plasma and slightly broadened unshifted symmetric emission lines.
5. Radiative wind shock predictions for an optically thin wind are consistent with the cool plasma and symmetric unshifted emission lines of σ Ori AB. However, the rather narrow line widths and low f/i ratios imply X-ray formation in slowly-moving plasma in the wind acceleration zone close to the star. It remains to be seen whether future numerical simulations of the line-driven instability mechanism can reproduce the narrow lines.
6. Other possible emission mechanisms for σ Ori AB that are not yet totally ruled out but remain speculative are: (i) a magnetically confined wind shock in the weak-field limit, and (ii) a sub-terminal speed colliding wind system if σ Ori A does have a spectroscopic companion. The MCWS scenario lacks solid observational support in the absence of any evidence for a magnetic field in σ Ori AB. More complete information about the properties of the putative spectroscopic companion and its orbit will be needed to make meaningful comparisons of colliding wind theory with observations.

We thank Ms. Victoria Swisher for assistance with data analysis and Dr. Stephen Drake for providing information on *VLA* observations of σ Ori. This research was supported by grants GO5-6009X (SAO) and NNG05GE69G (NASA GSFC).

REFERENCES

- Abbott, D.C. 1982, *ApJ*, 259, 282
- Anders, E. & Grevesse, N. 1989, *Geochim. Cosmochim. Acta*, 53, 197
- Babel, J. & Montmerle, T. 1997a, *A&A*, 323, 121 (BM97a)
- Babel, J. & Montmerle, T. 1997b, *A&A*, 485, L29
- Berghöfer, T.W. & Schmitt, J.H.M.M. 1994, *A&A*, 290, 435
- Berghöfer, T.W. & Schmitt, J.H.M.M., & Cassinelli, J.P. 1996, *A&AS*, 118, 481
- Bessell, M.A. & Brett, J.M. 1988, *PASP*, 100, 1134
- Blumenthal, G.R., Drake, G.W.F., & Tucker, W.H. 1972, *ApJ*, 172, 205
- Bolton, C.T. 1974, *ApJ*, 192, L7
- Borra, E.F. & Landstreet, J.D. 1979, *ApJ*, 228, 809
- Caballero, J.A. 2005, *Astron. Nachr.*, 326, 1007
- Caballero, J.A. 2007a, *A&A*, 466, 917
- Caballero, J.A. 2007b, *Astron. Nachr.*, 328 (No. 3-4), 1
- Caballero, J.A. 2008, *MNRAS*, 383, 750
- Cassinelli, J.P., Cohen, D.H., MacFarlane, J.J., Sanders, W.T., & Welsh, B.Y. 1994, *ApJ*, 421, 705
- Cassinelli, J.P., Miller, N.A., Waldron, W.A., MacFarlane, J.J., & Cohen, D.H. 2001, *ApJ*, 554, L55
- Cassinelli, J.P. & Olson, G.L. 1979, *ApJ*, 229, 304
- Cohen, D.H., Cassinelli, J.P., & Macfarlane, J.J. 1997, *ApJ*, 487, 867
- Cohen, D.H., Cooper, R.G., Macfarlane, J.J., Owocki, S.P., Cassinelli, J.P., & Wang, P. 1996, *ApJ*, 460, 506
- Cohen, D.H., de Messières, G.E., MacFarlane, J.J., Miller, N.A., Cassinelli, J.P., Owocki, S.P., & Liedahl, D.A. 2003, *ApJ*, 586, 495

- Cohen, D.H., Kuhn, M.A., Gagné, M., Jensen, E.L.N., & Miller, N.A. 2008, MNRAS, in press (arXiv:0802.4084v1)
- Drake, S.A. 1990, AJ, 100, 572
- Edwards, T.W. 1976, AJ, 81, 245
- Feldmeier, A., Kudritzki, R.-P., Palsa, R. Pauldrach, A.W.A., & Puls, J. 1997, A&A, 320, 899
- Feldmeier, A., Puls, J., & Pauldrach, A.W.A. 1997, A&A, 322, 878
- Franciosini, E., Pallavicini, R., & Sanz-Forcada, J. 2006, A&A, 446, 501 (FPS06)
- Gabriel, A.H. & Jordan, C. 1969, MNRAS, 145, 241
- Gagné, M. et al. 2005, ApJ, 628, 986
- Gatti, T., Natta, A., Randich, S., Testi, L., & Sacco, G. 2008, A&A, in press (arXiv:0801.2886)
- Getman, K.V. et al. 2005, ApJS, 160, 319
- Gorenstein, P. 1975, ApJ, 198, 95
- Groote, D. & Hunger, K. 1997, A&A, 319, 250
- Groote, D. & Schmitt, J.H.M.M. 2004, A&A, 418, 235
- Hernández, J. et al. 2007 ApJ, 662, 1067
- Howarth, I.D. & Prinja, R.K. 1989, ApJS, 69, 527
- Hunger, K., Heber, U., & Groote, D. 1989, A&A, 224, 57
- Ignace, R., Oskinova, L.M., & Foullon, C. 2000, MNRAS, 318, 214
- Jeffries, R.D. 2007, MNRAS, 376, 1109
- Kahn, S.M. et al. 2001, A&A, 365, L312
- Kenyon, S.J. & Hartmann, L. 1995, ApJS, 101, 117
- Kramer, R.H., Cohen, D.H., & Owocki, S.P. 2003, ApJ, 592, 532
- Krolik, J.H. & Raymond, J.C. 1985, ApJ, 298, 660

- Landstreet, J.D. & Borra, E.F. 1978, *ApJ*, 224, L5
- Lanz, T. & Hubeny, I. 2007, *ApJ*, 169, 83
- Lee, T.A. 1968, *ApJ*, 152, 913
- Leutenegger, M.A., Paerels, F.B.S., Kahn, S.M., & Cohen, D.C. 2006, *ApJ*, 650, 1096
- Lucy, L.B. 1982, *ApJ*, 255, 286
- Lucy, L.B. & White, R.L. 1980, *ApJ*, 241, 300
- Luo, D., McCray, R., & MacLow, M.-M. 1990, *ApJ*, 362, 267
- MacFarlane, J.J., Cassinelli, J.P., Welsh, B.Y., Vedder, P.W., Vallergera, J.V., & Waldron, W.L. 1991, *ApJ*, 380, 564
- Mason, B.D., Gies, D.R., Hartkopf, W.I., Bagnuolo, W.G., Brummelaar, T.T., & McAlisster, H.A. 1998, *AJ*, 115, 821
- Mayne, N.J., Naylor, T., Littlefair, S.P., Saunders, E.S., & Jeffries, R.D. 2007, *MNRAS*, 375, 1220
- Miller, N.A., Cassinelli, J.P., Waldron, W.L., MacFarlane, J.J., & Cohen, D.H. 2002, *ApJ*, 577, 951
- Menten, K.M., Reid, M.J., Forbrich, J., & Brunthaler, A. 2007, *A&A*, 474, 515
- Morrell, N. & Levato, H. 1991, *ApJS*, 75, 965
- Ness, J.-U., Brickhouse, N.S., Drake, J.J., & Huenemoerder, D.P. 2003, *ApJ*, 598, 1277
- Oliveira, J.M., Jeffries, R.D., van Loon, J. Th., & Rushton, M.T. 2006, *MNRAS*, 369, 272
- Owocki, S.P., Castor, J.I., & Rybicki, G.B. 1988, *ApJ*, 335, 914
- Owocki, S.P. & Cohen, D.H. 2001, *ApJ*, 559, 1108
- Pauldrach, A.W.A., Kudritzki, R.P., Puls, J., Butler, K., & Hunsinger, J. 1994, *A&A*, 283, 525
- Perryman, M.A.C. et al. 1997, *A&A*, 323, L49
- Porquet, D. 2005, in *X-Ray Diagnostics of Astrophysical Plasmas*, ed. R.K. Smith (American Inst. of Physics), 177

- Porquet, D., Mewe, R., Dubau, J., Raassen, A.J.J., & Kaastra, J.S., 2001 *A&A*, 376, 1113
- Pradhan, A.K. 1982, *ApJ*, 263, 477
- Preibisch, T. & Feigelson, E.D. 2005, *ApJS*, 160, 390
- Preibisch, T. et al. 2005, *ApJS*, 160, 401
- Press, W.H., Teukolsky, S.A., Vetterling, W.T., & Flannery, B.P. 1992, *Numerical Recipes in Fortran: The Art of Scientific Computing* (2nd ed.; New York: Cambridge Univ. Press), 617
- Reiners, A., Stahl, O., Wolf, B., Kaufer, A., & Rivinius, T. 2000, *A&A*, 363, 585
- Rieke, G.H. & Lebofsky, M.J. 1985, *ApJ*, 288, 618
- Runacres, M.C. & Owocki, S.P. 2002, *A&A*, 381, 1015
- Sandstrom, K.M., Peek, J.E.G., Bower, G.C., Bolatto, A.D., & Plambeck, R.L. 2007, *ApJ*, 667, 1161
- Sanz-Forcada, J., Franciosini, E., & Pallavicini, R. 2004, *A&A*, 421, 715
- Savage, B.D., Massa, D., Meade, M., & Wesselius, P.R. 1985, *ApJS*, 59, 397
- Schulz, N.S., Canizares, C.R., Huenemoerder, D., & Lee, J.C. 2000, *ApJ*, 545, L135
- Sherry, W.H., Walter, F.M., & Wolk, S.J. 2004, *AJ*, 128, 2316 (S04)
- Skinner, S.L., Brown, A., & Stewart, R.T. 1993, *ApJS*, 87, 217
- Skinner, S.L., Zhekov, S.A., Palla, F., & Barbosa, C.L.D.R. 2005, *MNRAS*, 361, 191
- Smith, R.K., Brickhouse, N.S., Liedahl, D.A., & Raymond, J.C. 2001, *ApJ*, 556, L91
- Stelzer, B. et al. 2005, *ApJS*, 160, 557
- Stevens, I.R., Blondin, J.M., & Pollock, A.M.T. 1992, *ApJ*, 386, 265
- Townsend, R.H.D., Owocki, S.P., & Groote, D. 2005, *ApJ*, 630, L81
- Townsend, R.H.D., Owocki, S.P., & ud-Doula, A. 2007, *MNRAS*, 382, 139
- ud-Doula, A. & Owocki, S.P. 2002, *ApJ*, 576, 413
- van Loon, J. Th. & Oliveira, J.M. 2003, *A&A*, 405, L33

Vogt, N. 1976, *A&A*, 53, 9

Waldron, W. & Cassinelli, J.P. 2001, *ApJ*, 548, L45

Waldron, W., Corcoran, M.F., Drake, S.A., & Smale, A.P. 1998, *ApJS*, 118, 217

Walter, F.M., Wolk, S.J., Freyberg, M., & Schmitt, J.H.M.M. 1997, *Mem. Soc. Astr. Ital.*, 68, 1081

Wolk, N.R., Wolk, S.J., Walter, F.M., & Sherry, W.H. 2006, in *Protostars and Planets V*, eds. B. Reipurth, D. Jewitt, & K. Keil (U. of Arizona Press: Tucson), 8425

Zapatero Osorio, M.R. et al. 2002, *A&A*, 384, 937

Table 1. σ Ori AB Properties^a

		Reference
Spectral Type	O9.5V + B0.5V	(1)
Distance (pc) ^b	352 $^{+166}_{-85}$	(2)
V (mag)	3.80 - 3.81	(3),(4),(5)
E(B–V) (mag)	0.05 - 0.07 ^c	(3),(4),(5)
T _{eff} (K)	33,000	(6)
R _* (R _⊙)	9	(6)
log \dot{M} (M _⊙ yr ^{−1})	−7.1	(6)
v _∞ (km s ^{−1})	1060	(6)
log [L _* /L _⊙]	4.9	(6)
log L _{wind} (ergs s ^{−1}) ^d	34.4	(6)
log L _x (ergs s ^{−1})	31.5	(7)
log [L _x /L _*]	−7.0	(7)

^a Notes: σ Ori = HD 37468. L_x is the unabsorbed value in the 0.5 - 7 keV range. Refs. (1) Edwards 1976; (2) *Hipparcos* (Perryman et al. 1997); (3) Lee 1968; (4) Savage et al. 1985; (5) Vogt 1976; (6) Howarth & Prinja 1989; (7) this work (0.5 - 7 keV).

^bWe adopt d = 352 pc in this work. A distance d = 334 $^{+25}_{-22}$ pc was determined by Caballero (2008), who also noted that d ~ 385 pc is possible if the system is a triple.

^cAdopting A_V ≈ 3E(B–V) = 0.15 - 0.21 mag gives N_H = (3.3 - 4.7) × 10²⁰ cm^{−2} using the Gorenstein (1975) conversion.

^dL_{wind} = $\dot{M}v_{\infty}^2/2$.

Table 2. Chandra X-ray Sources in the Vicinity of σ Ori AB^a

CXO No.	R.A. (J2000)	Decl. (J2000)	Net Counts (cts)	$\langle E \rangle$ (keV)	K_s (mag)	Identification(offset) (arcsec)
1	05 38 29.12	-02 36 03.0	69±8(v)	1.58	11.69	2M053829.12-023602.7(0.30)
2	05 38 31.43	-02 36 33.8	7±3	1.29	10.99	2M053831.41-023633.8(0.24)
3	05 38 31.57	-02 35 14.7	32±6	2.07	10.35	2M053831.58-023514.9(0.24)
4	05 38 32.83	-02 35 39.4	147±12	1.35	10.73	2M053832.84-023539.2(0.30)
5	05 38 33.34	-02 36 18.3	21±5	1.41	11.11	2M053833.36-023617.6(0.72)
6	05 38 34.04	-02 36 37.2	8±3	1.10	11.08	2M053834.06-023637.5(0.42)
7	05 38 34.31	-02 35 00.2	50±7	1.29	10.35	2M053834.31-023500.1(0.12)
8	05 38 35.21	-02 34 38.1	369±19(v)	3.01	...	M07:053835.22-023438.0(0.18)
9	05 38 38.22	-02 36 38.6	390±20(v)	1.79	10.31	2M053838.22-023638.4(0.18)
10	05 38 38.48	-02 34 55.2	697±26(v)	1.60	9.12	2M053838.49-023455.0(0.24)
11	05 38 39.72	-02 40 19.2	12±4(v)	3.09	12.88	2M053839.73-024019.7(0.54)
12	05 38 41.21	-02 37 37.4	29±5	3.40	14.04	2M053841.23-023737.7(0.48)
13	05 38 41.28	-02 37 22.7	323±18	1.64	10.59	2M053841.29-023722.6(0.24)
14	05 38 41.35	-02 36 44.6	14±4	1.13	12.08	2M053841.35-023644.5(0.12)
15	05 38 42.27	-02 37 14.5	9±3	2.56	10.77	2M053842.28-023714.7(0.30)
16	05 38 43.01	-02 36 14.7	6±3	1.93	10.63	2M053843.02-023614.6(0.18)
17	05 38 43.85	-02 37 07.3	16±4	1.38	11.77	2M053843.87-023706.9(0.54)
18	05 38 44.22	-02 40 20.0	158±13	1.52	10.44	2M053844.23-024019.7(0.30)
19	05 38 44.76	-02 36 00.3	2514±50	0.86	4.49	2M053844.76-023600.2(0.12); σ Ori AB
20	05 38 44.83	-02 35 57.4	43±7(v)	1.37	...	σ Ori IRS1
21	05 38 45.35	-02 41 59.6	50±5	1.69	11.04	2M053845.37-024159.4(0.42)
22 ^c	05 38 46.82	-02 36 43.5	6±2	0.95	12.35	2M053846.85-023643.5(0.48)
23	05 38 47.19	-02 35 40.5	454±21(v)	1.56	6.95	2M053847.20-023540.5(0.18); σ Ori E
24	05 38 47.46	-02 35 25.4	87±9	1.64	10.72	2M053847.46-023525.3(0.18)
25	05 38 47.89	-02 37 19.6	188±14(v)	2.20	10.78	2M053847.92-023719.2(0.54)
26	05 38 48.27	-02 36 41.2	42±7	1.35	11.14	2M053848.29-023641.0(0.30)
27	05 38 48.68	-02 36 16.4	106±10(v)	1.35	11.17	2M053848.68-023616.2(0.18)
28	05 38 49.12	-02 41 23.9	22±6	1.62	...	S04:053849.14-024124.8 (0.96)
29	05 38 49.17	-02 38 22.5	112±11	1.32	10.51	2M053849.17-023822.2(0.24)
30	05 38 49.69	-02 34 52.6	8±3	1.22	12.09	2M053849.70-023452.6(0.24)
31	05 38 50.02	-02 37 35.5	15±4	1.64	12.10	2M053850.03-023735.5(0.18)
32 ^{b,c}	05 38 50.16	-02 36 54.6	5±2	4.06
33	05 38 51.43	-02 36 20.7	53±7	1.86	11.55	2M053851.45-023620.6(0.36)
34	05 38 51.75	-02 36 03.3	6±3	1.56	12.03	2M053851.74-023603.3(0.18)
35	05 38 51.85	-02 33 33.0	17±4	2.94
36	05 38 53.03	-02 38 53.7	12±4	1.50	10.83	2M053853.07-023853.6(0.61)
37	05 38 53.37	-02 33 23.2	863±29(v)	1.67	9.73	2M053853.37-023323.0(0.24)
38	05 38 58.24	-02 38 51.5	25±5	2.67
39	05 38 59.03	-02 34 13.2	13±4	2.73
40	05 38 59.51	-02 35 28.6	12±4	3.06
41	05 39 00.53	-02 39 38.7	94±10	1.66	11.11	2M053900.53-023939.0(0.30)
42	05 39 01.47	-02 38 56.5	342±19	1.42	8.09	2M053901.50-023856.4(0.36); HD 37525 ^d

^a Notes: X-ray data are from CCD7 (ACIS chip S3) using events in the 0.5 - 7 keV range. Tabulated quantities are: running source number, X-ray position (R.A., decl.), net counts and net counts error from *wavdetect* (accumulated in a 90,967 s exposure, rounded to the nearest integer, background subtracted and PSF-corrected), mean photon energy $\langle E \rangle$, K_s magnitude of near-IR 2MASS counterpart, and 2MASS (2M ...) or optical (S04 = Sherry, Walter, & Wolk 2004; M07 = Mayne et al. 2007) candidate counterpart identification within a 2'' search radius. The offset (arc seconds) between the X-ray and counterpart position is given in parentheses. A (v) following Net Counts error indicates that the source is likely variable as indicated by a variability probability $P_{var} \geq 0.95$ determined from the Kolmogorov-Smirnov (KS) statistic. All sources were confirmed to be present in the archived 98 ksec *Chandra* HRC-I image (Obsid 2560).

^b Probable *XMM-Newton* counterpart is source NX 99 in Table B.1 of Franciosini et al. (2006). High value of $\langle E \rangle$ suggests possible extragalactic background source.

^c Low-significance *wavdetect* detection (2. < significance < 3.).

^d Double star with a B5V primary and a companion at separation 0.''45 (Caballero 2005).

Table 3. Spectral Fits of Zero-Order ACIS-S3 CCD Spectra^a

CXO No.	N_{H} (10^{20} cm $^{-2}$)	kT_1 (keV)	kT_2 (keV)	norm_1 (10^{-5})	norm_2 (10^{-5})	χ^2/dof (χ^2_{red})	Flux (10^{-13} ergs cm $^{-2}$ s $^{-1}$)
4	{3.0}	0.37 [0.23-0.51]	1.4 [1.2-1.7]	1.71 [0.67-2.27]	3.32 [2.38-3.99]	5.6/5 (1.12)	0.70 (0.76)
8	5.0 [3.8-8.8]	0.69 [0.47-2.16]	19.8 [8.1-...]	3.49 [0.10-13.6]	14.1 [12.4-17.4]	32.3/31 (1.04) ^b	1.97 (3.07)
9	1.5 [0.0-4.5]	0.61 [0.35-0.78]	2.5 [2.1-2.9]	2.14 [1.44-2.79]	10.4 [9.00-12.0]	31.2/31 (1.01)	1.87 (1.93)
10	2.5 [1.2-5.0]	0.70 [0.61-0.76]	2.4 [2.1-2.8]	5.81 [4.83-7.10]	14.4 [12.0-16.3]	72.8/52 (1.40)	3.19 (3.37)
13	{3.0}	0.74 [0.63-0.84]	3.1 [2.3-4.8]	2.58 [1.52-3.37]	7.19 [5.53-8.52]	11.4/11 (1.04)	1.55 (1.65)
18	{3.0}	0.37 [0.26-0.59]	2.0 [1.6-2.5]	1.89 [0.54-2.56]	3.73 [2.96-4.78]	13.1/14 (0.94)	0.78 (0.84)
19 ^c	{3.0}	0.30 [0.29-0.31]	...	111. [105.-116.]	...	76.5/49 (1.56)	15.4 (17.8)
19 ^c	{3.0}	0.21 [0.18-0.24]	0.47 [0.45-0.55]	79.9 [69.0-90.9]	41.4 [25.8-50.3]	45.6/47 (0.97)	16.6 (19.5)
20	{3.0}	0.61 [0.27-0.83]	2.2 [1.2-...]	0.59 [0.27-0.89]	0.61 [0.10-1.11]	1.2/6 (0.20)	0.21 (0.23)
23 ^d	{3.0}	0.72 [0.61-0.80]	2.4 [2.0-3.0]	4.43 [3.46-5.24]	8.46 [6.91-10.4]	28.6/24 (1.19)	2.09 (2.23)
25	{3.0}	3.20 [2.59-4.09]	...	6.96 [6.07-7.86]	...	18.1/17 (1.06)	0.96 (1.00)
27	{3.0}	0.66 [0.49-0.82]	2.2 [1.5-3.4]	1.24 [0.81-1.62]	1.79 [0.96-2.55]	6.4/7 (0.91)	0.50 (0.54)
29	{3.0}	0.67 [0.47-0.82]	1.6 [1.1-3.2]	1.29 [0.67-1.89]	1.71 [0.71-2.52]	7.0/8 (0.88)	0.52 (0.56)
37	2.1 [0.9-4.1]	0.75 [0.65-0.83]	2.3 [2.1-2.6]	6.02 [4.42-7.06]	24.9 [22.0-27.8]	26.2/32 (0.82)	4.59 (4.80)
42	{3.0}	0.76 [0.68-0.83]	2.6 [2.0-3.5]	4.69 [3.65-5.49]	5.56 [4.15-7.37]	34.4/29 (1.19)	1.76 (1.89)

^a Notes: The CXO no. in column (1) refers to Table 2. Fits are based on one-temperature (1T) or two-temperature (2T) optically thin plasma *apex* solar-abundance models of rebinned spectra in XSPEC (v. 12.3). Solar abundances are referenced to Anders & Grevesse (1989). The notation $N_{\text{H}} = \{3.0\}$ means the absorption column density was held fixed at that value during fitting. Brackets enclose 90% confidence intervals and an ellipsis means the algorithm used to compute the 90% confidence limit did not converge. The *norm* is related to the volume emission measure (EM) by $\text{EM} = 10^{14} 4\pi d_{cm}^2 \text{norm}$, where d_{cm} is the distance (cm) to the source. The total X-ray fluxes are the absorbed values in the 0.5-7 keV range, followed in parentheses by unabsorbed values.

^bAn absorbed power-law model with a photon power-law index $\alpha = +1.6$ [1.4 - 1.8] and $N_{\text{H}} = 2.5e20$ cm $^{-2}$ gives nearly identical fit statistics with $\chi^2/\text{dof} = 34.7/33$ and an unabsorbed flux $2.47e-13$ ergs cm $^{-2}$ s $^{-1}$.

^cEstimated zero-order photon pileup is 5% for σ Ori AB. Events with energies below 0.5 keV were excluded from the fit to avoid any possible contamination by soft UV/optical leaks.

^dA 3T *apex* model gives an improved fit with $N_{\text{H}} = 2.6$ [1.1-10.4] $\times 10^{20}$ cm $^{-2}$, $kT_1 = 0.24$ [0.09-0.39] keV, $kT_2 = 0.81$ [0.75-1.05] keV, $kT_3 = 2.6$ [2.1-3.3] keV, $\text{norm}_1 = 2.91$ [1.00-12.6]e-5, $\text{norm}_2 = 3.77$ [2.05-5.42]e-5, $\text{norm}_3 = 8.11$ [6.73-9.76]e-5, $\chi^2/\text{dof} = 18.6/21$ ($\chi^2_{red} = 0.89$), and Flux = 2.24 (2.41) $\times 10^{-13}$ ergs cm $^{-2}$ s $^{-1}$.

Table 4. σ Ori AB Emission Line Properties^a

Ion	λ_{lab} (Å)	λ_{obs} (Å)	$\Delta\lambda$ (mÅ)	Line Flux (10^{-5} ph cm $^{-2}$ s $^{-1}$)	HWHM (km s $^{-1}$)	log T $_{max}$ (K)
Si XIII(r)	6.6479	0.12 (0.01 - 0.22)	{300}	7.0
Mg XI(r)	9.1687	9.165 (9.162 - 9.169)	-4.	0.42 (0.30 - 0.55)	250 (8 - 374)	6.8
Mg XI(i)	9.2312	0.41 (0.27 - 0.52)	250 ^c	6.8
Mg XI(f)	9.3143 ^d	...	6.8
Ne X	10.239	0.25 (0.09 - 0.42)	{300}	6.8
Ne IX	11.544	0.48 (0.23 - 0.74)	{300}	6.6
Ne X ^b	12.132	12.127 (12.124 - 12.130)	-5.	1.64 (1.28 - 1.98)	390 (248 - 542)	6.8
Ne IX(r)	13.447	13.446 (13.441 - 13.449)	-1.	3.36 (2.80 - 4.03)	314 (216 - 381)	6.6
Ne IX(i)	13.553	13.546 (13.543 - 13.548)	-7.	3.53 (2.87 - 4.09)	314 ^c	6.6
Ne IX(f)	13.699 ^d	...	6.6
Fe XVII	15.014	15.013 (15.010 - 15.016)	-1.	7.94 (6.69 - 9.14)	279 (195 - 355)	6.7
O VIII	15.176	1.11 (0.53 - 1.98)	{300}	6.5
Fe XIX	15.198	1.01 (0.55 - 2.24)	{300}	6.9
Fe XVII	15.261	15.258 (15.251 - 15.266)	-3.	3.09 (2.36 - 3.83)	{300}	6.7
O VIII	16.006	16.009 (16.002 - 16.015)	+3.	2.63 (1.57 - 3.60)	195 (0 - 405)	6.5
Fe XVII	16.780	16.778 (16.772 - 16.785)	-2.	4.98 (3.66 - 6.27)	155 (21 - 278)	6.7
Fe XVII	17.051	17.049 (17.043 - 17.055)	-2.	5.32 (4.15 - 6.63)	163 (92 - 240)	6.7
Fe XVII	17.096	17.091 (17.086 - 17.096)	-5.	6.91 (5.58 - 8.29)	{163}	6.7
O VII	18.627	1.86 (0.25 - 3.46)	{300}	6.3
O VIII ^b	18.967	18.968 (18.964 - 18.972)	+1.	22.0 (19.6 - 27.8)	330 (273 - 435)	6.5
O VII(r)	21.602	21.608 (21.598 - 21.617)	+6.	15.5 (10.7 - 21.8)	298 (97 - 507)	6.3
O VII(i)	21.804	21.803 (21.796 - 21.810)	-1.	22.4 (15.2 - 30.1)	298 ^c	6.3
O VII(f)	22.098 ^d	...	6.3

^a Notes: X-ray data are from the background-subtracted HETG/MEG1 spectrum (+1 and -1 orders combined), regrouped to a minimum of 10 counts per bin. Parentheses enclose 1σ intervals. Tabulated quantities are: ion name (Ion) where r,i,f denote resonance, intercombination, and forbidden lines, laboratory wavelength of transition (λ_{lab}), measured wavelength (λ_{obs}), $\lambda_{obs} - \lambda_{lab}$ ($\Delta\lambda$), observed (absorbed) continuum-subtracted line flux (Line Flux), line half-width at half-maximum (HWHM), and maximum line power temperature (T $_{max}$). An ellipsis means that λ_{obs} was not measured due to faint or closely-spaced lines. Curly braces enclose quantities that were held fixed during fitting. The value of λ_{obs} is subject to the ± 11 mÅ absolute wavelength calibration accuracy of HETG/MEG.

^bBlend.

^cThe line width was allowed to vary during fitting but was kept equal to the width of the resonance (r) line.

^dThe forbidden line was undetected.

Table 5. σ Ori AB He-like Ion Line Flux Ratios^a

	Mg XI	Ne IX
$\lambda_{lab,r}$ (\AA)	9.1687	13.447 ^b
$\log T_{max}$ (K)	6.8	6.6
G^c	1.21 [0.76 - 1.92]	0.99 [0.73 - 1.32]
R^c	≤ 0.17	≤ 0.15
R_0	2.7	3.6
r_{fi}/R_*	≤ 1.8	≤ 4.4

^a The laboratory rest wavelength of the resonance line $\lambda_{lab,r}$ and the maximum line power temperature T_{max} are from APED. The line flux ratios $G = (f + i)/r$ and $R = f/i$ are from ISIS spectral fits (see below). R_0 is the theoretical limit of R at T_{max} for low photoexcitation and low density (Ne IX from Pradhan 1982; Mg XI from Porquet et al. 2001). The 90% confidence upper limit on the line formation radius is r_{fi}/R_* .

^bThe Ne IX resonance line may be weakly contaminated by emission from Fe XIX (13.462 \AA).

^cDetermined from simultaneous fits of MEG1+HEG1 spectra with ISIS. The He-like complexes were fitted allowing R , G , and the metal abundances to vary. ISIS applies the appropriate instrumental and thermal broadening to each line. The best-fit abundances of Mg and Ne are consistent with solar at the 90% confidence level. The continuum level was determined by a global 2T *vapex* fit of the zero-order spectrum. Square brackets enclose 90% confidence intervals on G and upper limits on R are 90% confidence.

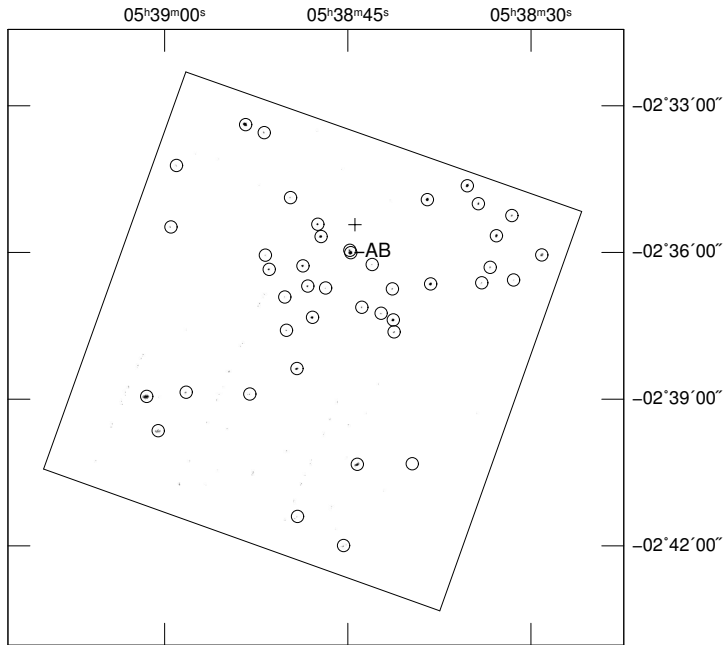


Fig. 1.— Circles mark the positions of the 42 X-ray sources detected on the ACIS-S3 CCD as listed in Table 2. A cross marks the *Chandra* aimpoint and the primary target σ Ori AB is identified.

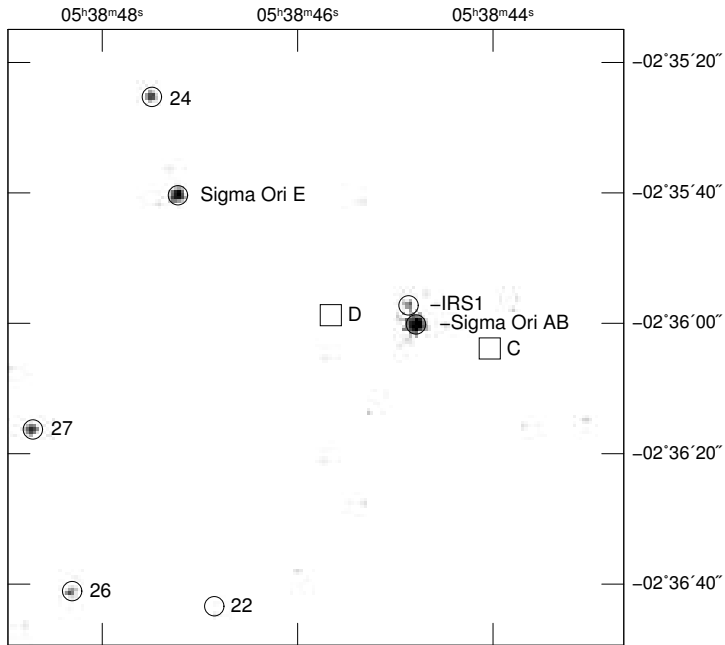


Fig. 2.— Unsmoothed ACIS-S3 image (0.5 - 7 keV) of the region near σ Ori AB. Circles mark ACIS-S3 detections and squares mark the optical positions of undetected stars σ Ori C and D. Numbered sources correspond to Table 2.

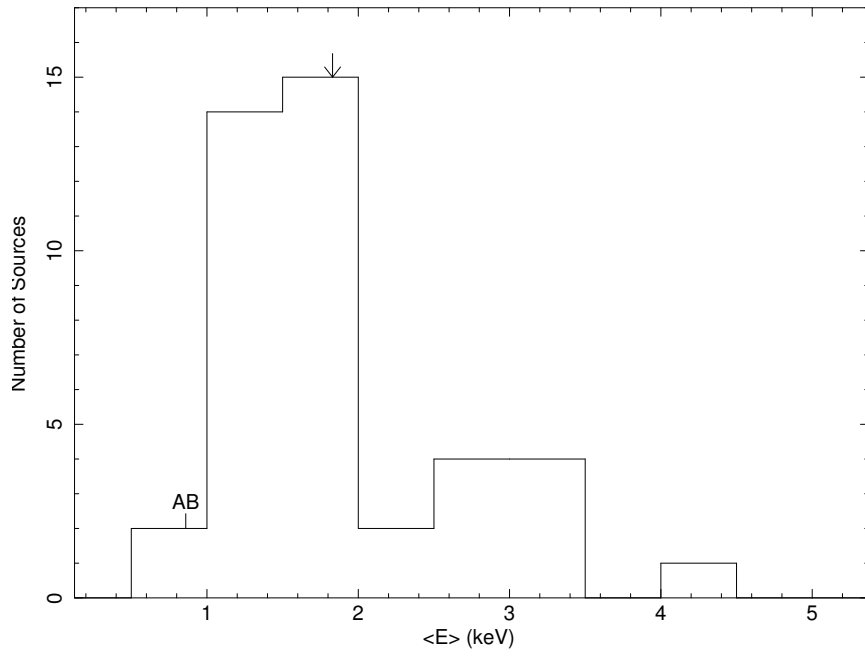


Fig. 3.— Histogram of mean photon energies for X-ray sources on ACIS-S3. The value of σ Ori AB is shown and the downward arrow marks the mean value.

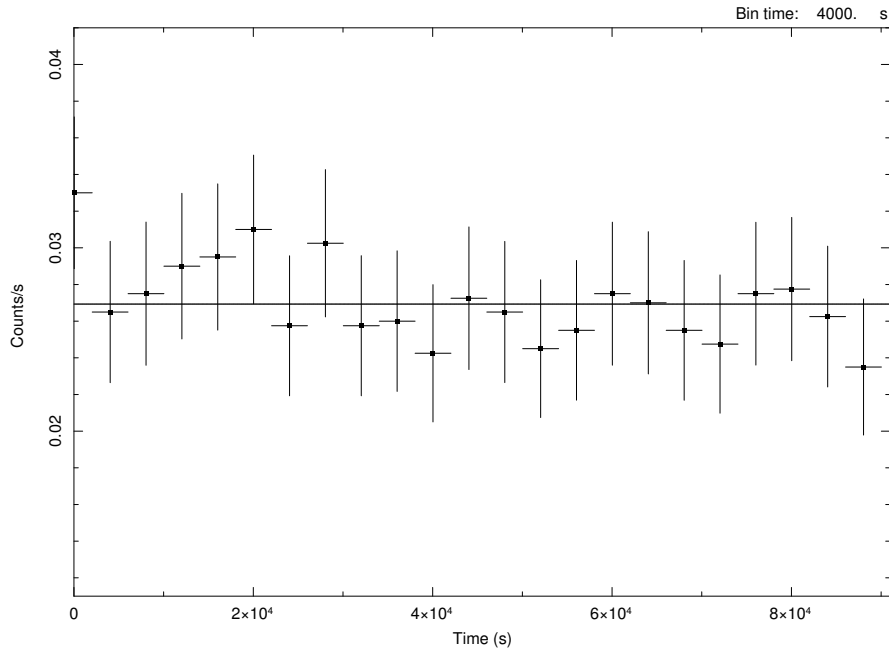


Fig. 4.— ACIS-S3 light curve of σ Ori AB (CXO 19) binned at 4000 s intervals using events in the 0.5 - 7 keV range and extraction radius $R_e = 1.''97$. The solid line is a best-fit constant count rate model. Error bars are 1σ . No statistically significant variability is detected.

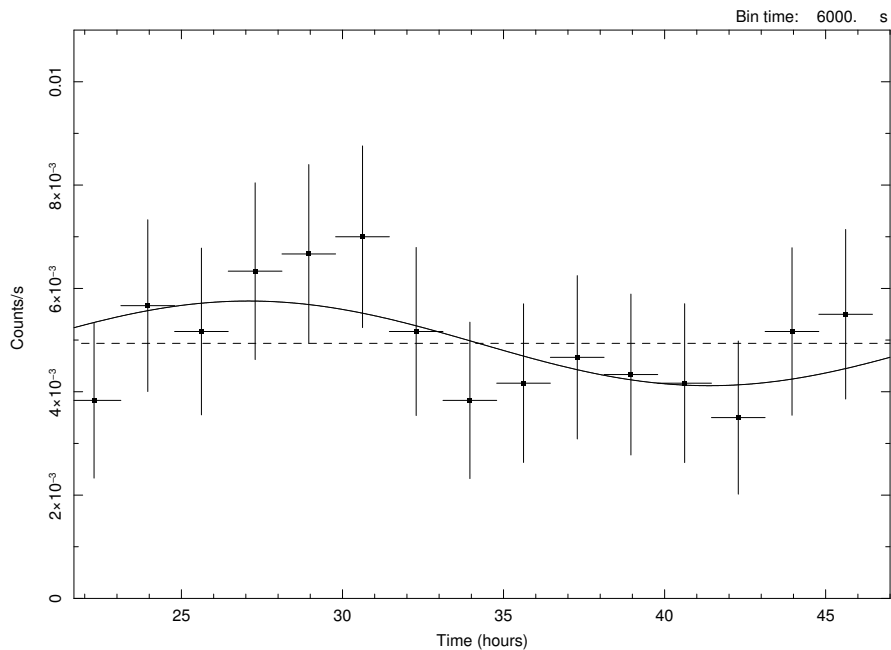


Fig. 5.— ACIS-S3 light curve of σ Ori E (CXO 23) binned at 6000 s intervals using events in the 0.5 - 7 keV range and extraction radius $R_e = 1.''97$. Error bars are 1σ . A KS test gives a low probability of constant count rate $P_{const} = 0.014$. The solid curve is a best fit sinusoid model with a constant offset of 0.004937 counts/s (dashed line) and the period fixed at the stellar rotation period $P_{rot} = 1.19084$ d = 28.58 hours. The time axis shows the elapsed time in hours from start of the day. The *Chandra* observation began at 20:59:02 UT on 2003 August 12 and spanned 1.053 d.

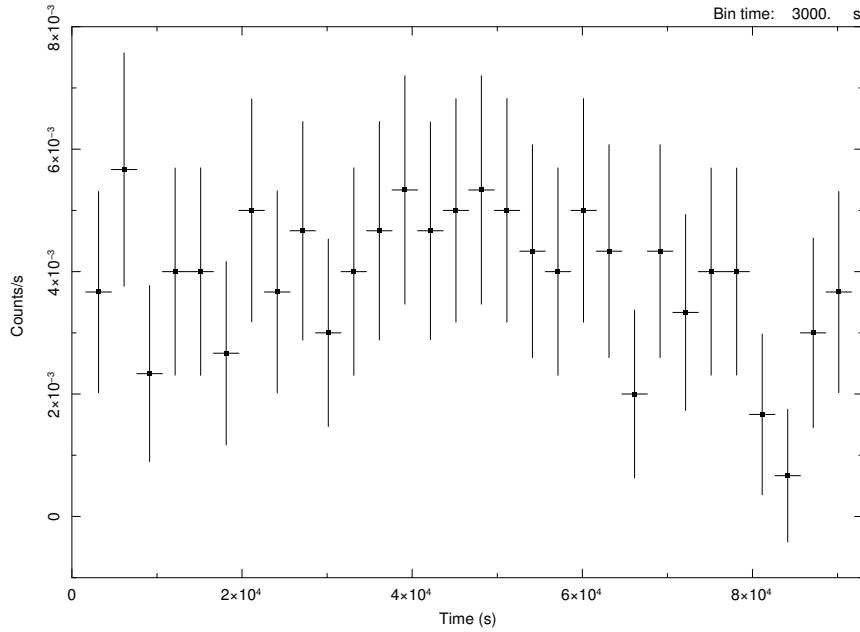


Fig. 6.— ACIS-S3 light curve of the variable source CXO J053835.21–023438.1 (CXO 8) binned at 3000 s intervals using events in the 0.5 - 7 keV range and extraction radius $R_e = 1.''97$. Error bars are 1σ . No *2MASS* counterpart was found but a faint $V = 20.88$ mag optical source lies at an offset of $0.''18$ from the X-ray position (Mayne et al. 2007).

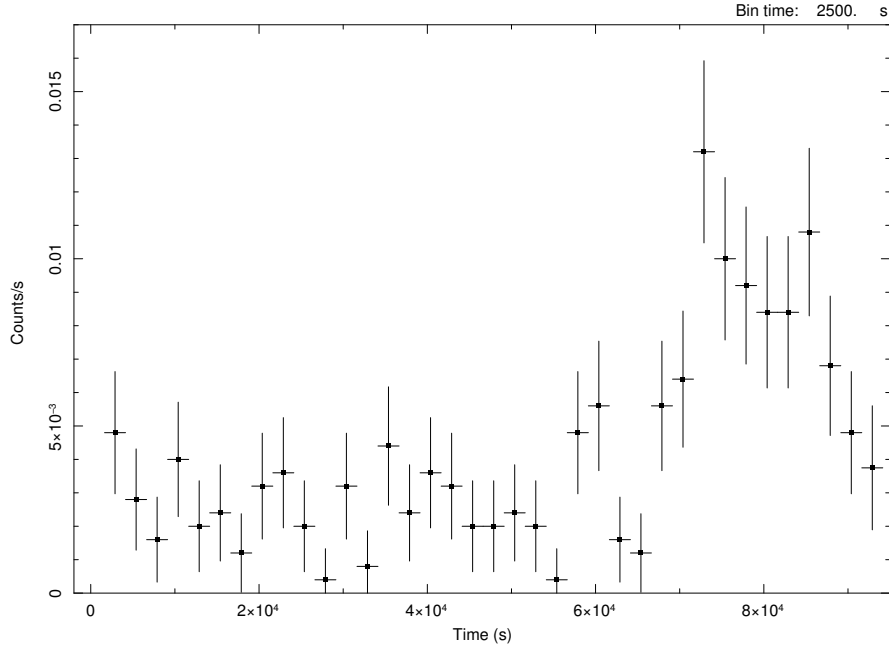


Fig. 7.— ACIS-S3 light curve of CXO J053838.22–023638.6 (CXO No. 9) binned at 2500 s intervals using events in the 0.5 - 7 keV range and extraction radius $R_e = 1.''97$. Error bars are 1σ . This T Tauri star shows weak $H\alpha$ emission and was classified as K8 by Zapatero Osorio (2002).

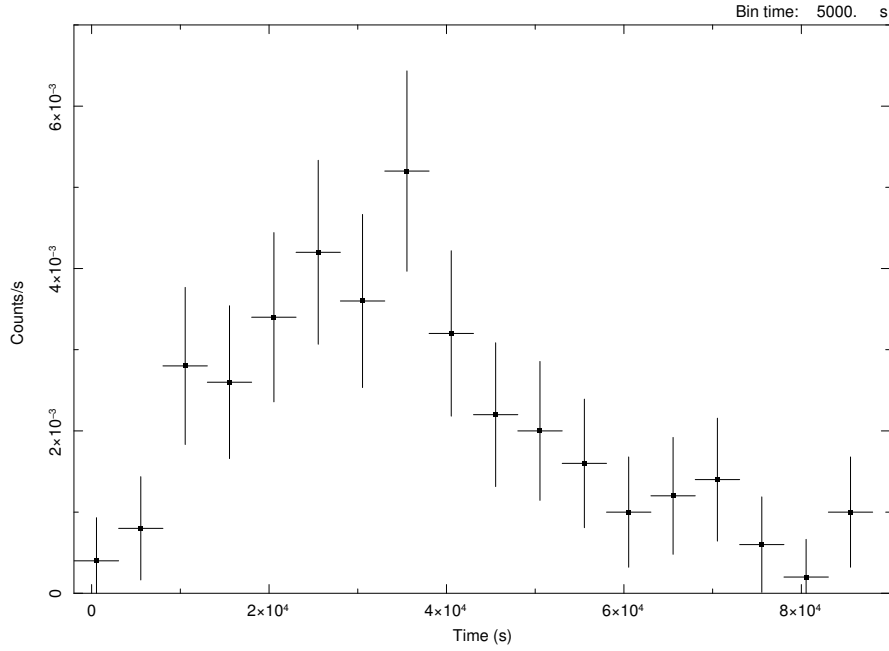


Fig. 8.— ACIS-S3 light curve of CXO J053847.89–023719.6 (CXO 25) binned at 5000 s intervals using events in the 0.5 - 7 keV range and extraction radius $R_e = 1.''97$. Error bars are 1σ . This star has been classified as M4 and shows a near-IR excess (Oliveira et al. 2006).

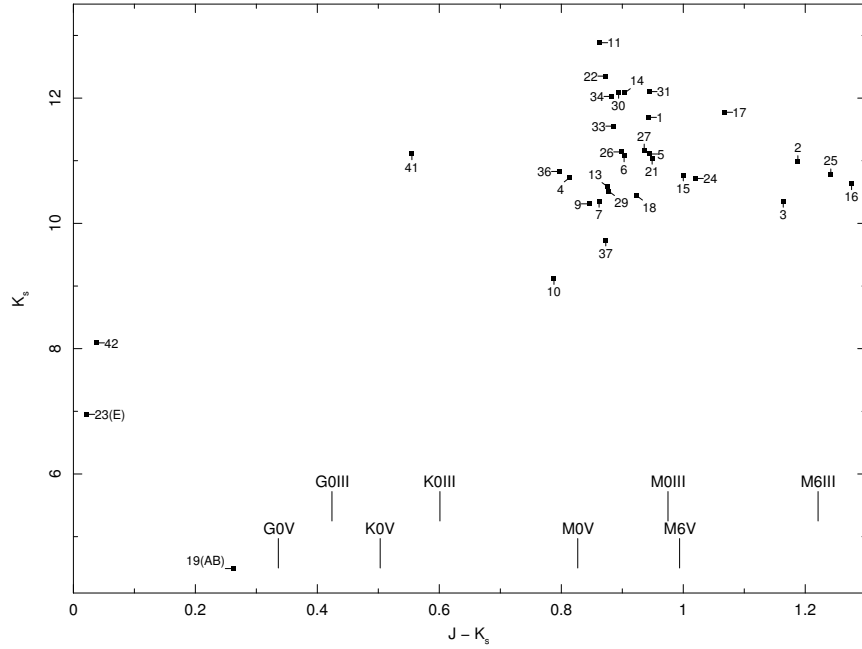


Fig. 9.— Color-magnitude diagram of X-ray sources on ACIS-S3 with 2MASS identifications. Source numbers correspond to Table 2. Intrinsic colors for late-type dwarfs and giants are from Bessell & Brett (1988). Source CXO 42 is the B5V star HD 37525. Source CXO 12 is not shown and lies off the right edge of the plot at $(J - K_s, K_s) = (2.33, 14.04)$.

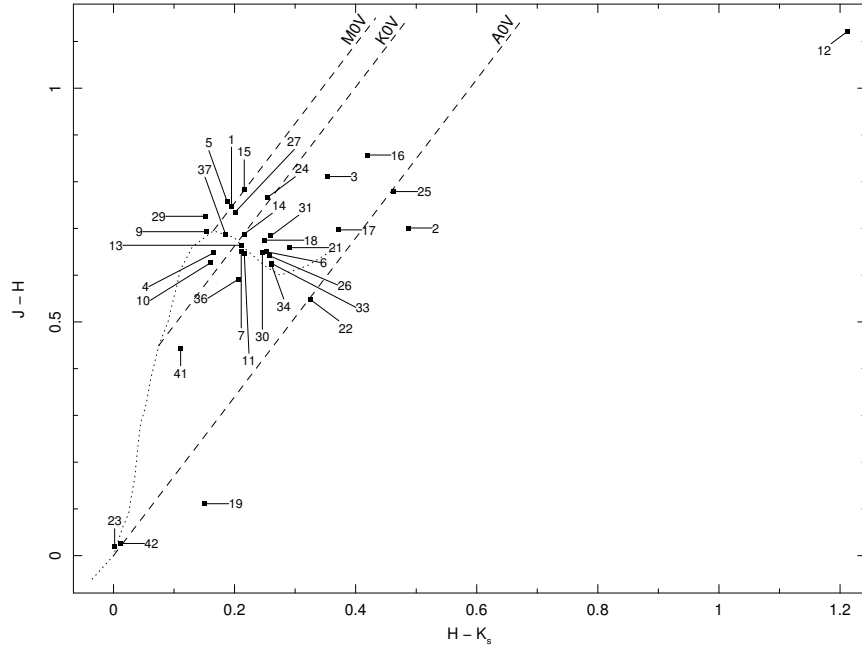


Fig. 10.— Color-color diagram of X-ray sources on ACIS-S3 with 2MASS identifications. Source numbers correspond to Table 2. The dotted line at left marks the unreddened main-sequence. The three sloping dashed lines show the loci of normally-reddened M0 V, K0 V, and A0 V stars, based on data from Bessell & Brett (1988) and Rieke & Lebofsky (1985).

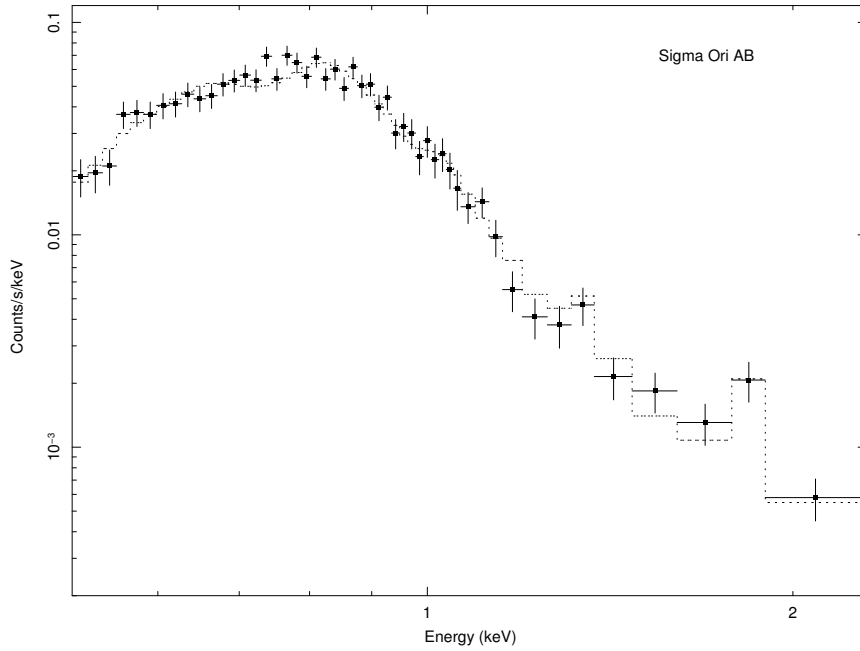


Fig. 11.— Zero-order CCD spectrum of σ Ori AB rebinned to a minimum of 20 counts per bin. The dotted line shows the best-fit 2T *apec* model with fit parameters as listed in Table 3.

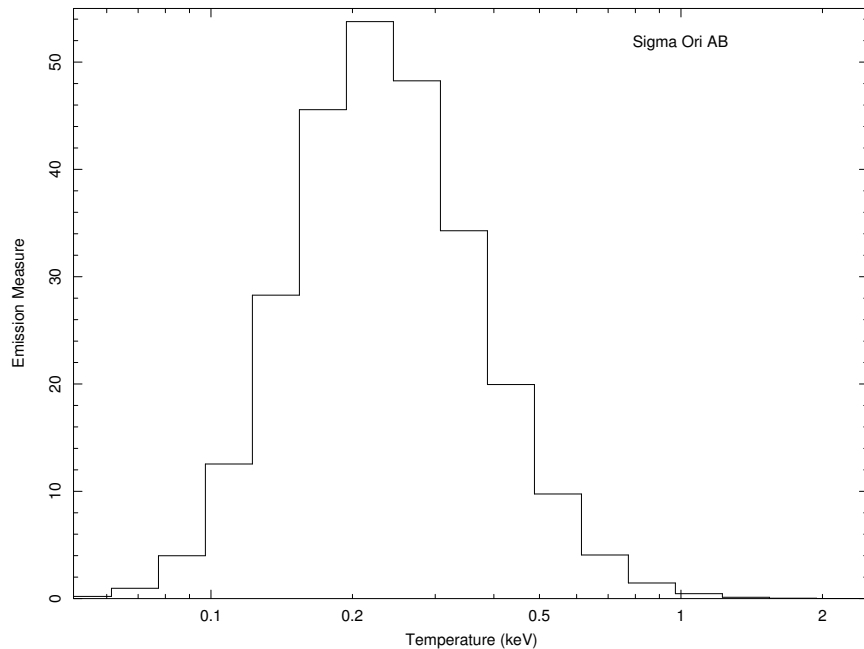


Fig. 12.— Emission measure distribution of σ Ori AB obtained from a best-fit of the zero-order CCD spectrum with the XSPEC model *c6pmekl* using solar abundances and hydrogen column density $N_{\text{H}} = 3 \times 10^{20} \text{ cm}^{-2}$.

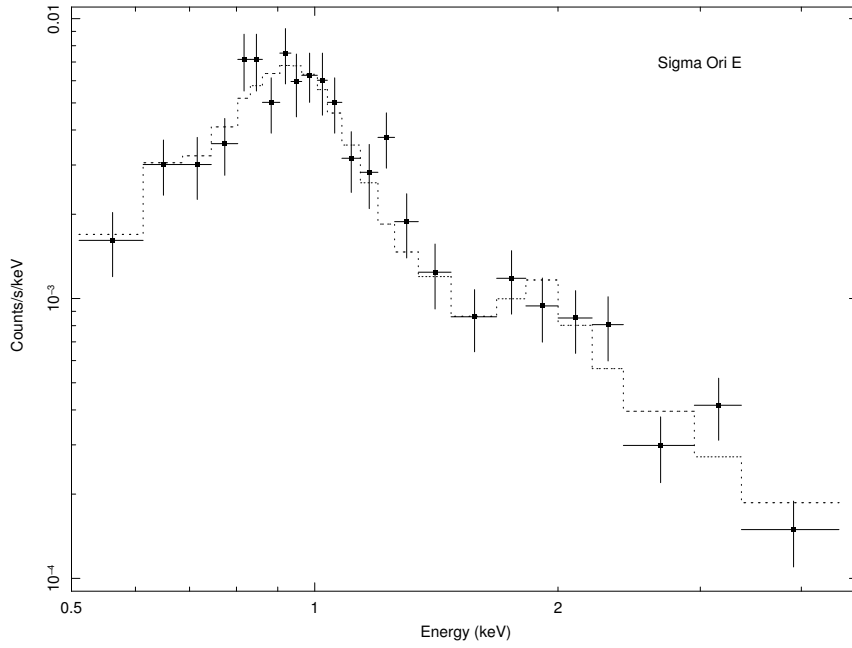


Fig. 13.— Zero-order CCD spectrum of σ Ori E rebinned to a minimum of 15 counts per bin. The dotted line shows the best-fit 3T *apec* model with fit parameters as listed in Table 3 notes.

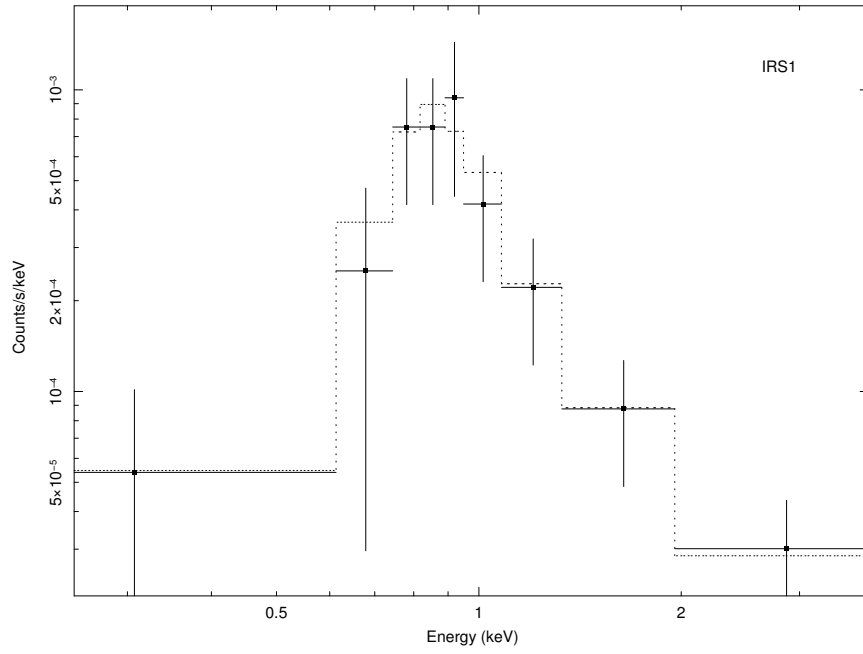


Fig. 14.— ACIS-S3 CCD spectrum of σ Ori IRS1 (CXO 20) binned to 5 counts per bin. The dotted line shows the 2T *apec* model with fit parameters as listed in Table 3.

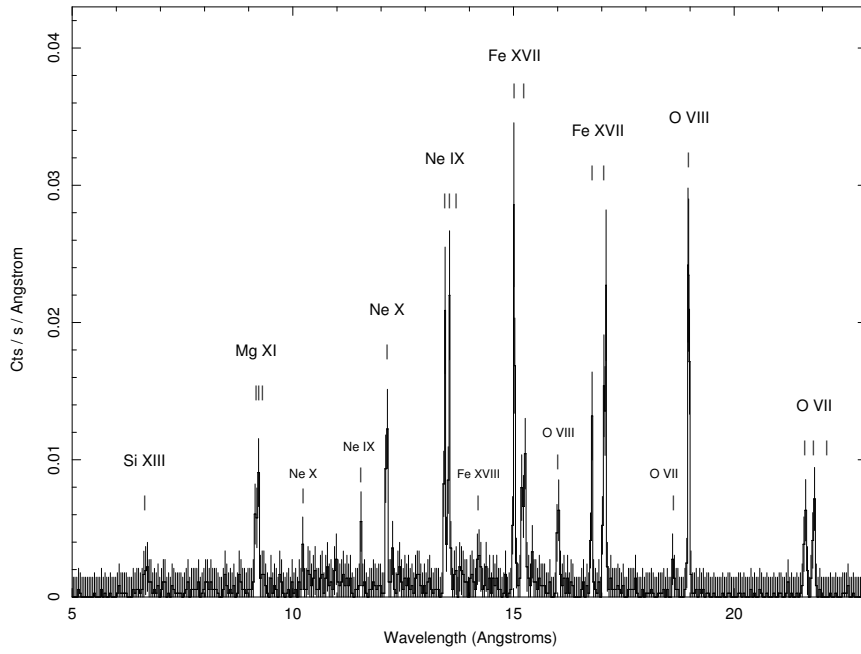


Fig. 15.— HETG/MEG1 background-subtracted spectrum (+1 and -1 orders combined; 1936 net counts) of σ Ori AB with prominent lines identified.

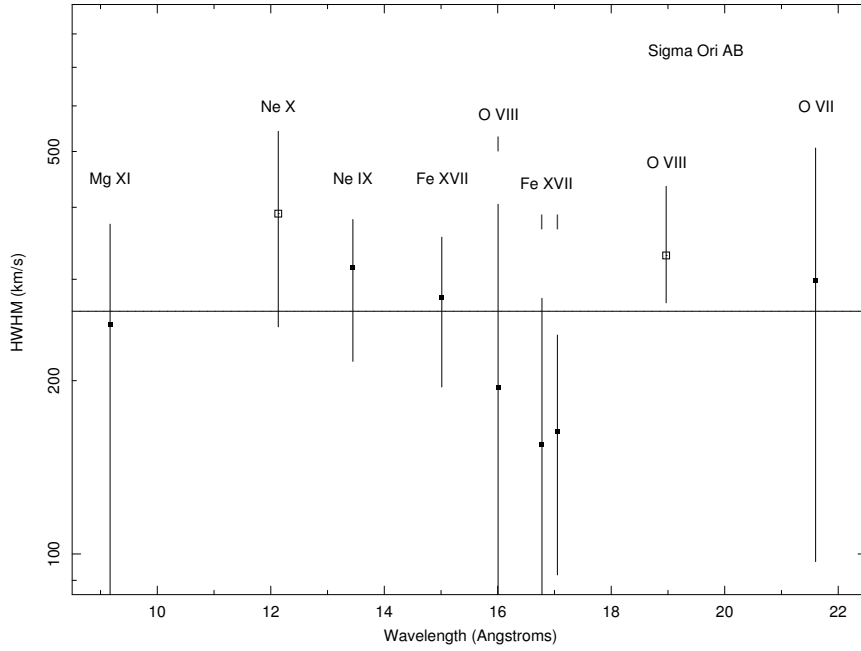


Fig. 16.— Measured line widths of σ Ori AB expressed as half-width at half-maximum (1σ error bars) versus line laboratory wavelength using data from Table 4. The two lines shown with open squares are blends and their HWHM values are likely overestimated. The solid horizontal line is the mean value $\overline{\text{HWHM}} = 264 \text{ km s}^{-1}$.

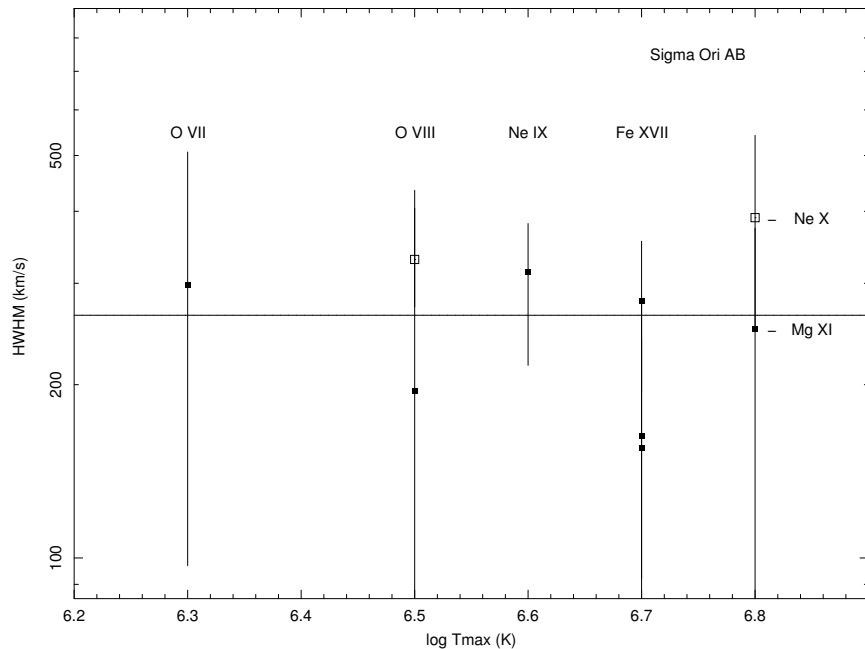


Fig. 17.— Measured line widths of σ Ori AB expressed as half-width at half-maximum (1σ error bars) versus maximum line power temperature T_{max} using data from Table 4. The two lines shown with open squares are blends and their HWHM values are likely overestimated. The solid horizontal line is the mean value $\overline{\text{HWHM}} = 264 \text{ km s}^{-1}$.

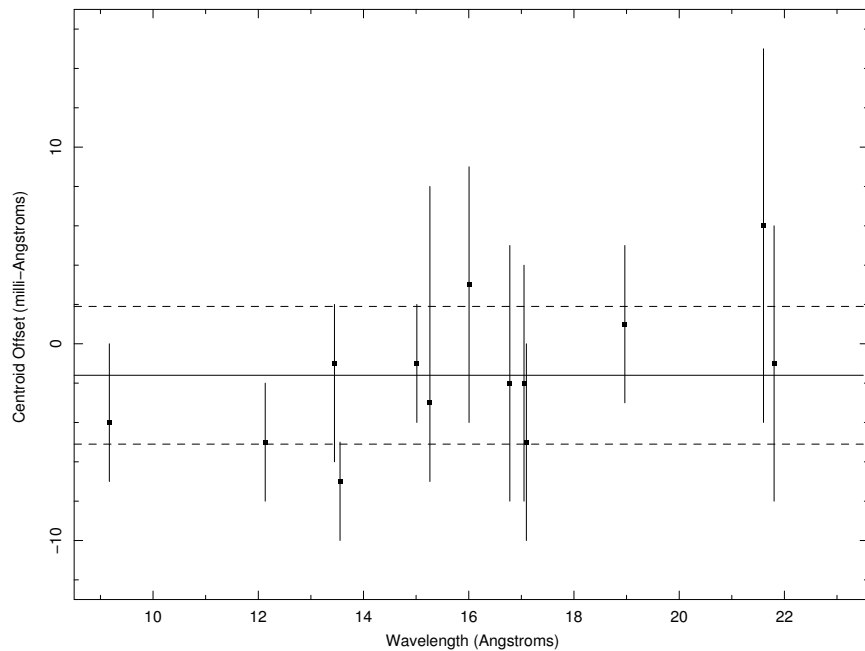


Fig. 18.— Plot of the centroid offset between the measured and laboratory line centroid of prominent lines in the MEG1 spectrum, using the offset values $\Delta\lambda = \lambda_{obs} - \lambda_{lab}$ from Table 4. Errors bars are 1σ . The mean offset (solid line) and $\pm 1\sigma$ uncertainty (dashed lines) for 13 measurements are $-1.6 (\pm 3.5) \text{ m}\text{\AA}$.

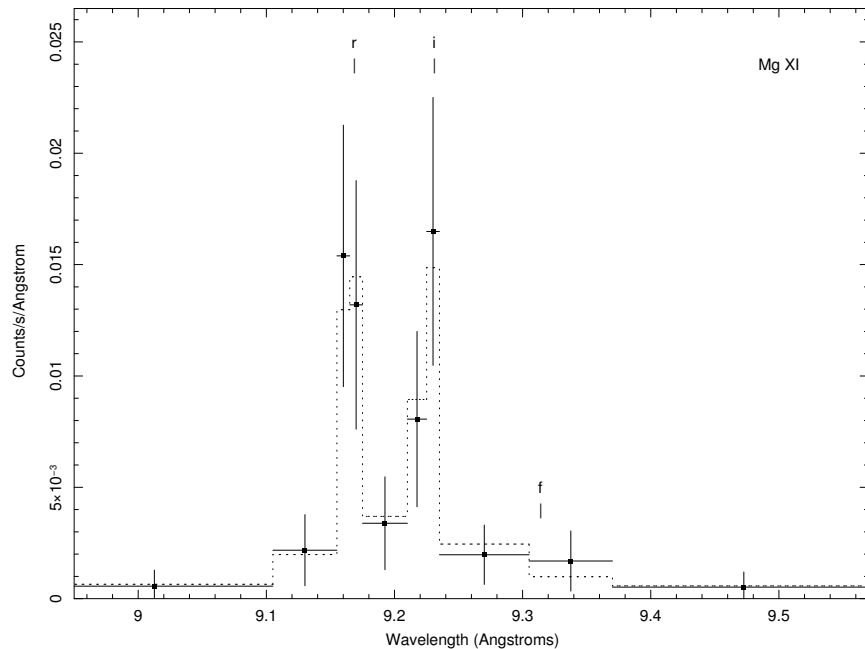


Fig. 19.— Histogram plot of the MEG1 spectrum (+1 and -1 orders combined) of σ Ori AB near the Mg XI He-like triplet, binned to a minimum of 10 counts per bin. Solid squares are data points and the dotted line is a Gaussian fit with weak power-law continuum. The resonance (r) and intercombination (i) lines are detected but the forbidden (f) line is not.

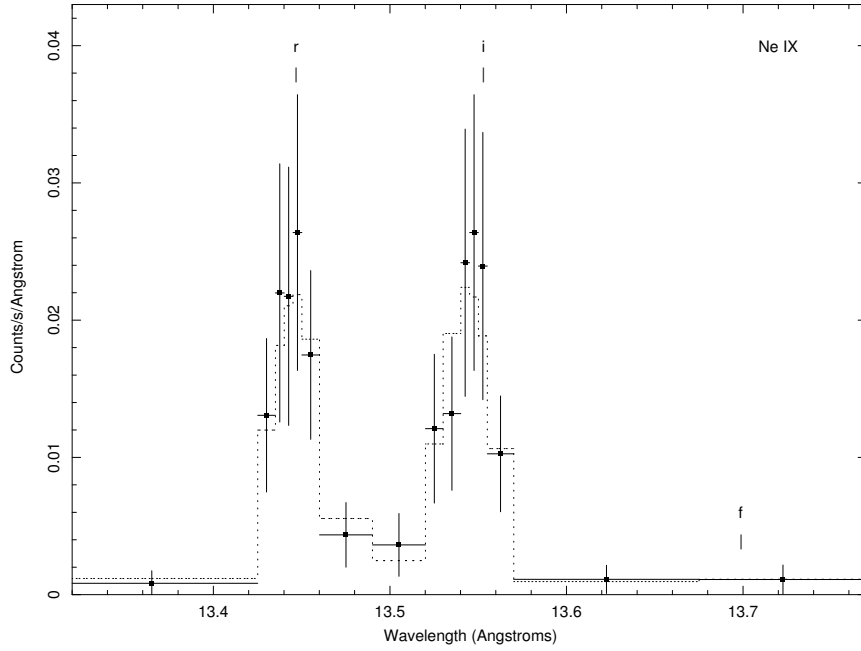


Fig. 20.— Histogram plot of the MEG1 spectrum (+1 and -1 orders combined) of σ Ori AB near the Ne IX He-like triplet, binned to a minimum of 10 counts per bin. Solid squares are data points and the dotted line is a Gaussian fit with weak power-law continuum. The resonance (r) and intercombination (i) lines are detected but the forbidden (f) line is not.

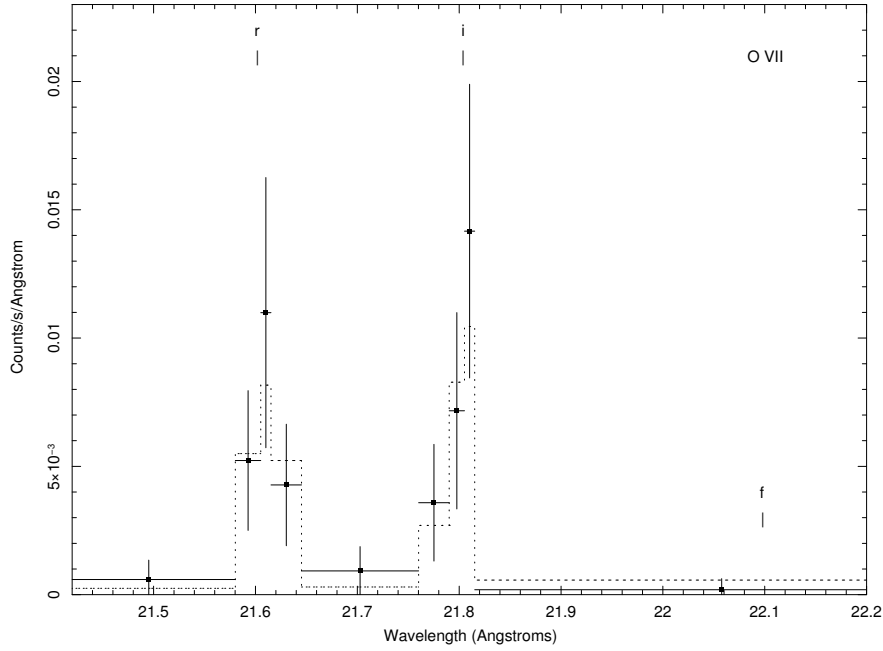


Fig. 21.— Histogram plot of the MEG1 spectrum (+1 and -1 orders combined) of σ Ori AB near the O VII He-like triplet, binned to a minimum of 10 counts per bin. Solid squares are data points and the dotted line is a Gaussian fit with weak power-law continuum. The resonance (r) and intercombination (i) lines are detected but the forbidden (f) line is not.

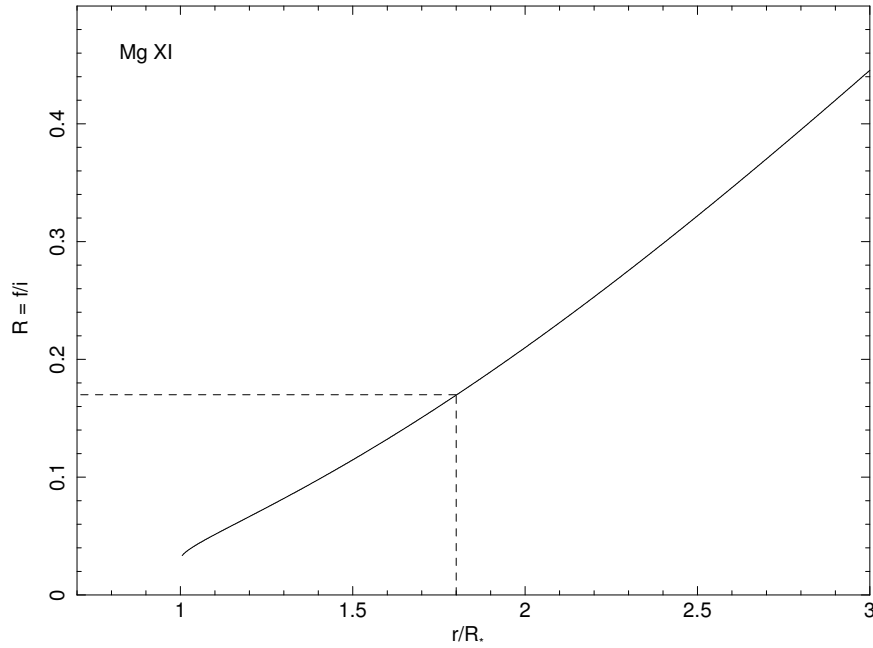


Fig. 22.— The ratio of forbidden-to-intercombination Mg XI line fluxes for σ Ori AB as a function of distance from the center of the star. The horizontal axis expresses the distance in units of the stellar radius, where $R_* = 9 R_\odot$. The solid line shows the predicted $R = f/i$ flux ratio based on a TLUSTY atmospheric model with $T_{eff} = 32,500$ K (see text). The vertical dashed line marks the 90% upper limit on the line formation radius $r_{fi} < 1.8 R_*$ based on the limit $R < 0.17$ determined from spectral fits (Table 5).